

Neoadjuvant androgen deprivation therapy with or without Fc-enhanced non-fucosylated anti-CTLA-4 (BMS-986218) in high risk localized prostate cancer: a randomized phase 1 trial

Casey R. Ager^{1,2,3,4,†}, Aleksandar Obradovic^{5,†}, Patrick McCann⁶, Matthew Chaimowitz², Alexander L. E. Wang⁵, Neha Shaikh⁷, Parin Shah⁷, Samuel Pan⁷, Caroline J. Laplaca⁸, Renu K. Virk⁹, Jessica C. Hill³, Collin Jugler³, Grace DeFranco³, Nilika Bhattacharya³, Howard I. Scher¹⁰, Guarionex Joel DeCastro⁸, Christopher B. Anderson⁸, James M. McKiernan⁸, Catherine S. Spina⁶, Mark N. Stein¹, Karie Runcie¹, Charles G. Drake^{1,8,15}, Andrea Califano^{5,7,11,12,13,14}, Matthew C. Dallos^{1,10}

¹ Department of Medicine, Division of Hematology and Oncology, Columbia University Irving Medical Center, New York, NY

² Columbia Center for Translational Immunology, Columbia University Irving Medical Center, New York, NY

³ Department of Immunology, Mayo Clinic Arizona, Scottsdale, AZ

⁴ Department of Urology, Mayo Clinic Arizona, Scottsdale, AZ

⁵ Department of Systems Biology, Vagelos College of Physicians and Surgeons, Columbia University Irving Medical Center, New York, NY

⁶ Department of Radiation Oncology, Columbia University Irving Medical Center, New York, NY

⁷ Herbert Irving Comprehensive Cancer Center, Columbia University Irving Medical Center, New York, NY

⁸ Department of Urology, Columbia University Irving Medical Center, New York, NY

⁹ Department of Pathology, Columbia University Irving Medical Center, New York, NY

¹⁰ Genitourinary Oncology Service, Department of Medicine, Memorial Sloan Kettering Cancer Center, New York, NY

¹¹ Department of Biochemistry & Molecular Biophysics, Vagelos College of Physicians and Surgeons, Columbia University Irving Medical Center, New York, USA 10032

¹² Department of Medicine, Vagelos College of Physicians and Surgeons, Columbia University Irving Medical Center, New York, USA 10032

¹³ Department of Biomedical Informatics, Vagelos College of Physicians and Surgeons, Columbia University Irving Medical Center, New York, USA 10032

¹⁴ Chan Zuckerberg Biohub New York, New York, NY, USA

¹⁵ Current Address: JnJ Innovative Medicine, Springhouse, PA

† These authors contributed equally

Running Title: Fc-Modified anti-CTLA-4 Depletes Tregs in Prostate Cancer

Keywords: Regulatory T Cell, CTLA-4, Ipilimumab, Prostate Cancer, Neoadjuvant, CyTOF, single cell RNA sequencing

Funding: This research was supported by National Institutes of Health (NIH) grants 1P50CA58236-15 and P30CA006973, the Prostate Cancer Foundation Challenge Grant, TJ Martell Foundation funds, and CUMC institutional funds to C.G.D, the NCI's Center for Cancer Systems Therapeutics (CaST) award U54CA274506, the NCI Outstanding Investigator award R35 CA197745, and the NIH Shared Instrumentation Grants S10 OD012351, S10 OD021764 and S10OD032433, to A.C., by a Prostate Cancer Foundation Young Investigator Award to M.D., by NIH grants UL1TR001873 and TL1TR001875, and institutional funds from Mayo Clinic to C.R.A., by NIH grant F30CA260765-01 to A.O., and by NIH/NIDDK grant T35DK093430 in support of A.L.E.W.

Correspondence: Dr. Matthew Dallos (dallosm@mskcc.org)

Conflicts of Interest: C.G.D is a co-inventor on patents licensed from Johns Hopkins University to BMS and Janssen. He is currently a paid employee of JnJ Innovative Medicine. A.C. is founder, equity holder, consultant, and director of DarwinHealth Inc., which has licensed IP related to these algorithms from Columbia University. Columbia University is an equity holder in DarwinHealth Inc.

Abstract

1 Men with high-risk localized prostate cancer exhibit high rates of post-surgical
2 recurrence. In these patients, androgen deprivation therapy (ADT) is
3 immunomodulatory, however increased infiltration of regulatory T cells (Tregs) may limit
4 the antitumor immune effects of ADT. We designed a neoadjuvant clinical trial to test
5 whether BMS-986218 – a next-generation non-fucosylated anti-CTLA-4 antibody
6 engineered for enhanced antibody-dependent cellular cytotoxicity or phagocytosis
7 (ADCC/P) – depletes intratumoral Tregs and augments the response to ADT. In this
8 single-center, two-arm, open-label study, 24 men with high-risk localized prostate
9 cancer were randomized to receive a single dose of ADT with or without two pre-
10 operative doses of BMS-986218 (anti-CTLA4-NF) prior to radical prostatectomy.
11 Treatment was well tolerated and feasible in the neoadjuvant setting. A secondary
12 clinical outcome was the rate of disease recurrence, which was lower than predicted in
13 both arms. Mechanistically, anti-CTLA4-NF reduced ADT-induced Treg accumulation
14 through engagement of CD16a/*FCGR3A* on tumor macrophages, and depth of Treg
15 depletion was quantitatively associated with clinical outcome. Increased intratumoral
16 dendritic cell (DC) frequencies also associated with lack of recurrence, and pre-clinical
17 data suggest ADCC/P-competent anti-CTLA-4 antibodies elicit activation and expansion
18 of tumor DCs. Patients receiving anti-CTLA4-NF also exhibited phenotypic signatures of
19 enhanced antitumor T cell priming. In total, this study provides the first-in-human
20 evidence of Treg depletion by glycoengineered antibodies targeting CTLA-4 in humans
21 and their potential in combination with ADT in prostate cancer patients with high-risk of
22 recurrence.

23 **Introduction**

24
25 To date, immune checkpoint blockade immunotherapy (ICB) has proven largely
26 ineffective for patients with prostate cancer (PCa)¹. Agents targeting the PD-1/PD-L1
27 pathway alone or in combination with androgen receptor inhibitors (KEYNOTE-164²,
28 KEYNOTE-991³, IMbassador250⁴), chemotherapy (KEYNOTE-921⁵), or PARP inhibition
29 (KEYLYNK-010⁶) have failed in phase III trials. Similarly, CTLA-4 blockade in a chemo-
30 naïve population (Ipi-095⁷) or post-docetaxel in combination with bone-targeted
31 radiation (Ipi-043⁸) did not meet pre-specified endpoints. However, long-term follow-up
32 on the Ipi-043 trial indicates a potential survival advantage of ipilimumab versus
33 placebo⁸. Furthermore, a phase II study of combination ipilimumab and nivolumab in
34 metastatic patients pre- or post-chemotherapy (CheckMate-650⁹) showed a survival
35 signal as compared to historical anti-PD-(L)1 monotherapy controls⁹. These findings
36 suggest that CTLA-4 blockade may possess clinical activity in PCa that warrants further
37 investigation, particularly if concerns regarding dose-dependent toxicity can be
38 addressed

39 One hypothesis explaining the relatively low efficacy of ICB in PCa is that baseline T
40 cell infiltration is insufficient for ICB to elicit robust T cell-mediated antitumor immunity¹.
41 Interestingly, our prior findings showed that standard of care androgen deprivation
42 therapy (ADT) initially increases CD8 T cell infiltration into primary PCa in both murine
43 models and patients^{10,11}. However, a counter-regulatory influx of immunosuppressive
44 CD4⁺FoxP3⁺ regulatory T cells (Tregs) inhibits the inflammatory effects of ADT,
45 implicating adaptive Treg resistance as a critical inhibitory mechanism^{10,11}. As such,
46 depletion of tumor-infiltrating Tregs (TI-Tregs) by anti-CTLA-4 antibodies with enhanced

47 antibody dependent cellular cytotoxicity or phagocytosis (ADCC/P) extends depth and
48 duration of response to androgen deprivation (ADT) in murine models, whereas non-
49 depleting anti-CTLA-4 antibodies and PD-1 blockade in the same setting is ineffective¹⁰.
50 These Fc-enhanced agents have also been hypothesized to have an improved
51 therapeutic index¹². Therefore, we reasoned that inhibiting TI-Treg number and/or
52 function in combination with ADT may effectively potentiate ICB efficacy in PCa.

53 Methods for depleting TI-Tregs have been studied thoroughly in pre-clinical models but
54 have as yet not been successfully validated in the clinic. Antibodies targeting cell
55 surface proteins enriched on TI-Tregs such as CTLA-4, CD25, CCR4, TIGIT, and CCR8
56 have either failed to show Treg depletion activity and/or efficacy in clinical trials or
57 remain under investigation¹³⁻¹⁶. We thus sought to further investigate anti-CTLA-4 in this
58 context, given its potential clinical activity in PCa⁸ and the fact that the first-generation
59 anti-CTLA-4 antibodies ipilimumab and tremelimumab were not optimized for Treg
60 depletion. Tremelimumab is a human IgG2 antibody with relatively low affinity for the
61 FcγRs such as CD16a (*FCGR3A*) that mediate ADCC/P, while Ipilimumab is a human
62 IgG1 isotype that can elicit ADCC/P. However, existing clinical data suggest ipilimumab
63 is a weak depleter, with evidence of Treg depletion restricted to patients with a high-
64 affinity germline polymorphic variant of *FCGR3A* (V158F)^{16,17}. To overcome this
65 limitation, antibodies targeting CTLA-4 bearing non-fucosylated Fc regions have been
66 recently developed to enhance binding to CD16a/*FCGR3A*, resulting in enhanced
67 ADCC/P¹⁸. However, it remains unclear whether non-fucosylated anti-CTLA-4
68 antibodies may be more effective in depleting TI-Tregs in patients. Furthermore,

69 whether these next-generation Fc-enhanced antibodies may overcome adaptive Treg
70 resistance following ADT is also unknown.

71 To address this challenge, we designed a randomized neoadjuvant clinical trial to
72 evaluate the safety, feasibility, clinical efficacy, and immunological activity of non-
73 fucosylated ipilimumab (BMS-986218; hereafter anti-CTLA4-NF) with ADT versus ADT
74 alone prior to surgery in men with high-risk localized prostate cancer (NeoRED-P;
75 NCT04301414). This window-of-opportunity trial enabled careful interrogation of the
76 immunological mechanisms of response to anti-CTLA4-NF through orthogonal
77 immunoprofiling by single cell RNA sequencing (scRNAseq), mass cytometry (CyTOF),
78 and spatial proteomics (multiplex immunofluorescence). We also leveraged the novel
79 RNA-seq-based pipeline PISCES to perform robust protein activity level assessment of
80 tumor microenvironment subpopulations and of their drug-mediated depletion, thus
81 bridging the transcriptomic and proteomic datasets. Pre-clinical validation studies in the
82 syngeneic MycCaP PCa model closely mirrored observed immunological correlates of
83 clinical response. Our findings demonstrate the tolerability and promising clinical activity
84 of ADT plus anti-CTLA4-NF in the neoadjuvant setting and provide a first-in-human
85 examination of whether Fc-engineered non-fucosylated anti-CTLA4 antibody variants
86 mediate TI-Treg depletion, while identifying additional putative mechanisms by which
87 anti-CTLA4-NF antibodies may augment antitumor immune responses in PCa.

88 **Results**

89

90 **Treatment Safety, Feasibility and Efficacy as Neoadjuvant Therapy in Prostate**

91 **Cancer**

92 Between February 26, 2020, and November 15, 2022, 24 patients were enrolled at
93 Columbia University Irving Medical Center. The first four patients received ADT with
94 degarelix acetate + anti-CTLA4-NF as a safety lead-in, after which 20 patients were
95 randomized 1:1 to ADT-only or ADT + anti-CTLA4-NF arms (Figure 1A). One patient in
96 the ADT + anti-CTLA4-NF arm did not receive surgery due to operating room closure
97 during SARS-CoV2 pandemic, and one patient in each arm was lost to follow-up (Figure
98 1B). For correlative studies, samples from a cohort of twelve stage- and grade-matched
99 treatment-naïve patients were collected as untreated controls. Baseline characteristics
100 of trial patients are summarized in Table 1. The arms were well balanced with respect to
101 age, race and ethnicity, pre-treatment serum PSA or testosterone, and rate of nodal
102 involvement or surgical margin involvement. Patients in the ADT + anti-CTLA4-NF arm
103 trended towards modestly higher grade group 5 disease and higher predicted
104 recurrence risk as measured by a validated risk nomogram (see Methods) than the ADT
105 alone arm. Tumor exome and mutational profiling of all patient-derived samples showed
106 12 patients with AR-V7 splice variants (38%), eight patients exhibiting TMRPSS2:ERG
107 fusion events (25%), four patients bearing mutated *TP53* (13%), three patients with
108 copy number loss or mutations in *PTEN* (9%), and two patients each with alterations *in*
109 *APC* and *CTNNB1* (6%; Extended Data Figure 1A). Of note, a single non-recurring
110 patient in the ADT + anti-CTLA4-NF arm was found to exhibit high tumor mutational
111 burden (TMB-H; 26 mutations/Mb), associated with a germline mutation in *MSH2*.

112 Treatment related adverse events (TRAE) of any grade were observed in 80% of ADT-
113 only patients and 71% of ADT + anti-CTLA4-NF patients, the most common events
114 were injection site reactions in both arms (Table 2). Three Grade 1-2 gastrointestinal
115 events were observed in patients receiving anti-CTLA4-NF. Severe treatment-related
116 adverse events (Grade \geq 3) were rare; a single patient in the ADT + anti-CTLA4-NF arm
117 exhibited a Grade 3 asymptomatic serum lipase elevation that resolved without
118 additional therapy and did not result in treatment discontinuation. No unexpected
119 surgical complications were observed, supporting a tolerable safety profile for the
120 addition of anti-CTLA4-NF to ADT in this patient population.

121 In the ADT-only arm, 80% of patients had an undetectable PSA at 12 months, with a
122 median recurrence-free survival of 1.61 years (IQR: 1.50–1.99 years) (Table 3). In the
123 ADT + anti-CTLA4-NF arm, 75% had an undetectable PSA at 12 months, with a median
124 recurrence-free survival of 1.82 years (IQR: 0.89–2.07 years) (Table 3). The overall
125 recurrence rate in patients treated with ADT + anti-CTLA4-NF was 29% (4 of 12
126 evaluable patients) and 20% (2 of 10 patients) in the ADT alone arm (Table 3). This
127 study was not powered to compare efficacy between treatment arms. However, after
128 predicting 2-year recurrence rates on a per-patient basis using a validated clinical risk
129 nomogram (Memorial Sloan Kettering Cancer Center Post-Radical Prostatectomy
130 Prediction; see Methods), we found both arms exceeded predicted 2-year recurrence-
131 free survival rates (Figure 1C-D). Patients in the ADT-only arm had a PSA50 response
132 rate prior to surgery of 33%, while patients in the ADT + anti-CTLA4-NF arm had a
133 PSA50 response rate of 54% ($p=0.4$; Table 3; Figure 1E-F). All patients recovered
134 testosterone to baseline levels within 6 months of prostatectomy (Extended Data Figure

135 2). Overall, these data suggest adding anti-CTLA4-NF to ADT is well-tolerated and
136 feasible in the neoadjuvant setting for patients with high-risk localized PCa.

137

138 **Anti-CTLA4-NF suppresses ADT-induced Treg expansion**

139 To elucidate the effects of ADT + anti-CTLA4-NF versus ADT alone versus no treatment
140 on prostate tumor-infiltrating immune populations, we performed transcriptomic and
141 proteomic-based immune profiling via paired scRNA sequencing (via 10X Genomics
142 droplet-based platform), mass cytometry (CyTOF), and immunofluorescence (IF; Figure
143 2A). Of the 36 patients assessed, 26 had scRNAseq data of sufficient quality, 25 had
144 CyTOF data of sufficient quality, and 29 had IF data of sufficient quality to be included in
145 further analyses (see Extended Data Figure 3A and methods for QC criteria and Figure
146 2B for a representative schematic). We first tested our secondary endpoint hypothesis
147 that anti-CTLA4-NF reduces TI-Treg density in ADT-treated PCa tumors by quantifying
148 the number of CD4⁺FoxP3⁺ Tregs per mm² in whole-tissue FFPE slides by IF (see
149 representative staining images in Figure 2C). For this analysis, we censored one patient
150 with MSI^{hi} status given the known association between MSI^{hi} status, high TMB, and
151 increased overall tumor T cell infiltration relative to MSI^{WT} patients¹⁹. In line with our
152 previous findings, we found ADT significantly increases Treg densities in the PCa tumor
153 parenchyma (p=0.001; Figure 2D). Concurrent treatment with ADT and anti-CTLA4-NF
154 resulted in a strong trend towards reduction in Treg density (p=0.06), indicating anti-
155 CTLA4-NF may have measurable Treg depletion activity.

156 To validate these results, we interrogated the immune TME of this cohort by scRNAseq
157 and CyTOF performed on independent, freshly processed prostatectomy specimens.

158 For scRNAseq data analysis we utilized the novel PISCES pipeline incorporating
159 unbiased Louvain-based clustering and metaVIPER (virtual inference of protein activity
160 by enriched regulon analysis²⁰) to quantitatively infer activity of approximately 6,500
161 regulatory proteins per cell²¹. Based on CITE-seq analysis and experimental validation,
162 this approach has been shown to outperform traditional gene expression-based
163 methods, wherein RNA dropout limits detection of key lineage- and function-determining
164 transcripts and reduces cluster resolution (see Methods for more detail and prior
165 studies²¹⁻²³ for pipeline validation). Integrating cells from all patients, we stratified
166 immune metaclusters corresponding to immune lineages including T/NK cells, B cells,
167 macrophage/DCs, monocytes, neutrophils, and plasma cells by PISCES and cross-
168 validated cluster identity at the gene expression level by parallel SingleR²⁴ and
169 supervised annotation (Figure 2E-F). Additionally, we identified stromal cell clusters
170 including fibroblasts, endothelial cells, megakaryocyte-erythroid progenitors (MEPs),
171 club/glandular cells, and four molecularly distinct epithelial tumor clusters. Tumor cell
172 clusters were validated by aberrant copy number analysis, using inferCNV^{25,26}
173 (Extended Data Figure 3B). In parallel, we performed semi-supervised FlowSOM²⁷
174 clustering followed by supervised UMAP embedding on all live CD45+ events from the
175 CyTOF dataset (Extended Data Figure 4A; see methods for workflow details). We
176 clearly resolved multiple immune populations using established lineage-defining protein
177 markers, including multiple T cell subsets, NK cells, monocytes, macrophage/DCs, and
178 neutrophils (Figure 2G-H). Further validating the PISCES-based stratification,
179 comparative analysis of immune lineages defined by both platforms revealed significant
180 immune subpopulation fraction correlations between scRNAseq and CyTOF for all

181 immune lineages on a per-patient basis. NK cells were a notable exception and were
182 not significantly correlated across platforms (Extended Data Fig 4B). Though correlated,
183 neutrophils were comparably underrepresented in the scRNAseq data relative to
184 CyTOF, as is common in droplet-based scRNAseq methodologies (Extended Data
185 Figure 3C-D). These data overall confirm faithful capture and annotation of relevant cell
186 types by both scRNAseq and CyTOF.

187 To test the hypothesis that anti-CTLA4-NF mediates intratumoral Treg depletion *in vivo*,
188 we first subclustered the scRNAseq T/NK cell metacluster to clearly resolve a Treg
189 cluster as validated by enrichment of established Treg transcriptional signature scores,
190 inferred activity of Treg lineage marker proteins by VIPER, and SingleR annotation
191 (Figure 2I-K). Mirroring the IF data, patients receiving ADT + anti-CTLA4-NF exhibited a
192 strong trending decrease in Treg frequency as compared to ADT alone ($p=0.06$; Figure
193 2L). In the CyTOF dataset, Tregs were clearly identified at the protein level in a
194 FlowSOM-derived cluster expressing the canonical $CD4^+CD25^+CD127^-FoxP3^+$
195 phenotype (Figure 2M) and additional markers indicative of tumor-infiltrating Tregs
196 including Helios, CCR8, TIGIT, CD39, and CCR4 (Figure 2N). Consistent with the
197 PISCES analyses and IF results, we observed a non-significant but consistent trend
198 towards a reduction in Treg frequency in the ADT + anti-CTLA4-NF arm compared to
199 the ADT alone arm (Figure 2O; $p=0.07$). Though the traditional significance threshold
200 was not reached by individual modalities, these data are highly consistent across three
201 independent immune profiling platforms in a small, prospectively treated patient cohort,
202 and thus suggest non-fucosylated anti-CTLA-4 antibody BMS-986218 may reduce
203 intratumoral Treg frequencies in prostate cancer.

204 **Increased depletion of phenotypically activated Tregs associates with clinical**
205 **response**

206 As our data suggests Treg depletion via anti-CTLA4-NF is limited in depth, we sought to
207 further validate and investigate the biological activity of anti-CTLA4-NF by interrogating
208 the molecular phenotype of residual Tregs in post-treatment tumors. We utilized the
209 CyTOF data for this analysis, as we captured an insufficient number of Tregs by
210 scRNAseq to permit rigorous subclustering of the TI-Treg compartment. Semi-
211 supervised FlowSOM subclustering and PaCMAP embedding of TI-Tregs in the CyTOF
212 dataset identified nine phenotypically distinct Treg subpopulations. These were primarily
213 resolved by differential expression of CD45RO, Ki67, granzyme B, CD39, CCR8, HLA-
214 DR, and/or 4-1BB (Figure 3A-C). This analysis revealed a potential phenotypic shift in
215 residual Tregs for patients treated with anti-CTLA4-NF, including a decrease in Tregs in
216 cluster Tr.5 defined by low CD39 expression, and increase in Tregs in cluster Tr.9, as
217 defined by high expression of 4-1BB and other activation markers (Figure 3D-E). To
218 validate these observations, we measured the fold change in geometric MFI (gMFI) of
219 all phenotypic markers in our CyTOF panel between Tregs in patients treated with ADT
220 versus patients treated with anti-CTLA4-NF (Figure 3F). We found Tregs remaining in
221 tumors after anti-CTLA4-NF exposure expressed the activation markers 4-1BB, CD39,
222 CCR8, CTLA-4, and CD25, suggesting that tumor-infiltrating Tregs remaining after anti-
223 CTLA4-NF are enriched for an activated phenotype (Figure 3F).

224 Given this observation, we next examined whether the depth of TI-Treg depletion
225 observed in treated patients associated with clinical response. For this, we stratified
226 patients that received ADT + anti-CTLA4-NF by recurrence (n=4) versus non-recurrence

227 (n=7) according to clinically annotated PSA recurrence within 2 years following surgery.
228 We limited this analysis to the scRNAseq dataset, as we did not capture CyTOF data for
229 all patients that recurred. We found that TI-Treg frequencies at time of surgery were
230 significantly higher in patients that went on to recur as compared to those that did not
231 recur (p=0.03; Figure 3G). In contrast, no other lymphocyte subset was significantly
232 associated with clinical outcome (Extended Data Figure 4E). In addition, we stratified
233 patients that received ADT + anti-CTLA4-NF by TI-Treg frequency and found that
234 patients with high TI-Treg frequencies exhibited significantly shorter time-to-recurrence
235 as compared to patients with low TI-Treg frequencies (p=0.0008; Figure 3H). There
236 were insufficient recurrence events in the ADT alone arm to perform a statistical
237 analysis of time-to-recurrence in ADT-treated patients stratified by TI-Treg frequency,
238 though no trend was observed (Extended Data Figure 4F). In agreement with this data,
239 it is unlikely TI-Treg frequency in absence of anti-CTLA4-NF would associate with
240 recurrence in this setting as prior studies show no association between Treg frequency
241 and recurrence risk in localized PCa²⁸. These correlative findings thus suggest that
242 depth of TI-Treg depletion is associated with response to ADT + anti-CTLA4-NF in
243 patients with high-risk localized prostate cancer.

244 **Efficiency of myeloid-mediated Treg depletion associates with duration of** 245 **response to therapy**

246 Given the putative association between anti-CTLA4-NF-mediated TI-Treg depletion and
247 clinical response, we next sought to investigate potential mechanisms for TI-Treg
248 depletion. In pre-clinical models, antibody-mediated Treg depletion by anti-CTLA4
249 canonically requires interactions between the anti-CTLA4 Fc region and activating

250 FcγRs such as CD16a (*FCGR3A*) on tumor-associated macrophages (TAMs)^{29,30}. To
251 determine whether macrophage FcγR expression was associated with Treg depletion
252 efficiency in response to ADT + anti-CTLA4-NF, we first annotated macrophage
253 populations in the scRNAseq dataset by both supervised manual annotation and
254 through systematic testing of established prostate cancer macrophage gene expression
255 signatures³¹ (Figure 4A-C). We identified 3 putative macrophage subsets: a recently
256 described prostate-specific MT⁺ macrophage subset³¹ and two subsets of TAMs defined
257 by TREM2 and CD206 (*MRC1*), respectively. Of these, TREM2⁺ and CD206⁺ TAMs
258 exhibited highest predicted protein activity for multiple FcγRs (Figure 4D), and TREM2⁺
259 TAMs showed the highest activity of the activating FcγR CD16a/*FCGR3A* (Figure 4E).
260 To test the hypothesis that anti-CTLA4-NF depletes Tregs through CD16a/*FCGR3A* on
261 TAMs, we examined whether CD16a/*FCGR3A* protein activity was correlated with
262 intratumoral TI-Treg frequencies on a per-patient basis. We found predicted
263 CD16a/*FCGR3A* protein activity across all myeloid subsets to be significantly correlated
264 with reduced Treg frequencies in ADT + anti-CTLA4-NF patients (p=0.033; Figure 4F).
265 In contrast, we found no significant correlation between myeloid CD16a/*FCGR3A*
266 protein activity and TI-Treg frequencies in patients who received ADT alone (p=0.223;
267 Figure 4F), supporting the hypothesis that CD16a/*FCGR3A* mediates TI-Treg depletion
268 in the context of treatment with anti-CTLA4-NF. We also found similar correlations
269 between TI-Treg frequencies and CD16a/*FCGR3A* activity within the TREM2⁺ TAMs
270 specifically (Figure 4G). These findings support the notion that TI-Treg depletion by anti-
271 CTLA4-NF is at least partially mediated through canonical tumor macrophage FcγR
272 interactions in the human PCa tumor microenvironment.

273 **Intratumoral dendritic cell frequencies associate with response to ADT + anti-**
274 **CTLA4-NF**

275
276 Overall, myeloid frequencies were not significantly altered by treatment (Figure 4H).
277 After stratification of ADT + anti-CTLA4-NF patients by recurrence status, however, we
278 observed intratumoral dendritic cell (DC) frequencies at time of surgery trended towards
279 higher abundance in patients that did not recur ($p=0.06$; Figure 4I). We thus stratified
280 patients by DC frequency at time of surgery and found those with fewer tumor-infiltrating
281 DCs exhibited a significantly shorter time to recurrence ($p=0.029$; Figure 4J). To further
282 investigate this novel association between DC frequencies and anti-CTLA4-NF
283 response, we returned to the MycCaP pre-clinical model of castration-sensitive prostate
284 cancer where we previously assessed mechanistic effects of ADCC-competent versus
285 ADCC-incompetent anti-CTLA4 antibodies in combination with ADT¹⁰. We implanted 8–
286 10-week-old male FVB mice with syngeneic Myc-CaP prostate tumors and performed
287 chemical castration with degarelix acetate (ADT) when tumors averaged $\sim 200\text{mm}^3$ in
288 volume (Figure 4K). Mice received a single dose of ADT alone or in combination with
289 three doses of anti-CTLA-4 (clone 9D9; 5 mg/kg) administered IP at three-day intervals.
290 To confirm Treg depletion was mediated through Fc γ R-dependent ADCC, mice
291 received either Fc-competent antibody (mIgG2a; anti-CTLA4 [D]) or the equivalent
292 clone and isotype bearing a mutation that nullifies Fc γ R interactions³² (mIgG2a-
293 LALAPG; anti-CTLA4 [ND]). These data were consistent with our prior findings that anti-
294 CTLA4 (D), but not anti-CTLA4 (ND), augments response to ADT in the Myc-CaP model
295 (Figure 4L-M). Following treatment, tumors and draining lymph nodes were harvested
296 and profiled by 45-parameter spectral flow cytometry, and data was analyzed by semi-
297 supervised FlowSOM clustering and supervised UMAP or unsupervised PaCMAP

298 embedding for visualization (Figure 4N; Extended Data Fig 5A-B). Consistent with
299 patient data, ADT + anti-CTLA4 (D) significantly reduced Treg frequencies compared to
300 ADT and ADT + anti-CTLA4 (ND) groups, indicating robust antibody-dependent Treg
301 depletion ($p=0.0031$; Figure 4O, top). We further found that animals treated with ADT +
302 anti-CTLA4 (D) exhibited significantly greater frequencies of tumor-infiltrating CD11c⁺
303 MHC-II^{hi} DCs compared to those receiving ADT or ADT + anti-CTLA4 (ND) ($p=0.0009$;
304 Figure 4O). Systematic subclustering of the tumor DC compartment revealed a striking
305 phenotypic shift in DCs in response to anti-CTLA4 (D) (Figure 4P, Extended Data Fig
306 5C-D). While DC phenotypes in mice treated with ADT or ADT + anti-CTLA4 (ND) were
307 enriched for canonical cDC1 and cDC2 markers such as CD103 or CD11b, respectively,
308 nearly all DCs in mice treated with anti-CTLA-4 (D) expressed PD-L2, a marker of the
309 DC3 subset and/or mRegDC (mature DC enriched in immunoregulatory molecules)
310 program. The mRegDC phenotype is induced upon tumor antigen uptake, and
311 mRegDCs are thought to possess a unique role in shaping antitumor immune
312 responses³³. The increase in PD-L2⁺ DCs was unique to mice receiving anti-CTLA4 (D)
313 (Figure 4Q, Extended Data Fig 5E). Taken together, these data indicate ADCC/P
314 competent antibodies targeting CTLA-4 modulate tumor-infiltrating DCs, and that an
315 increased DC frequency following treatment with anti-CTLA4-NF is associated with
316 positive clinical outcome.

317

318 **ADT + anti-CTLA-4-NF enhances antitumor T cell priming**

319 Given the observed effects of anti-CTLA4-NF therapy on tumor Treg frequencies and
320 myeloid phenotypes, we next sought to interrogate the effect of ADT + anti-CTLA4-NF
321 on CD8 T cell responses in the tumor. For enhanced resolution of CD8 phenotypes in

322 the scRNAseq data, we first refined the previously compiled CD8-1 and CD8-2 clusters
323 (Figure 2K), removing a contaminating cell population presenting low *Cd8a* expression,
324 moderate *Cd4* expression, and an otherwise naïve gene signature (Extended Data Fig
325 6A-B). Subcluster analysis of the curated CD8 T cells resulted in an optimal three
326 cluster solution (Figure 5A). Utilizing established pan-cancer CD8 T cell gene signatures
327 from Zheng *et al.*³⁴ and prostate CD8 T cell signatures from Tuong *et al.*³¹ we annotated
328 these clusters as central memory (IL7R⁺ memory signature enrichment, prostate CD8
329 memory T cell signature enrichment, expression of CCR7), effector memory
330 (enrichment of GZMK⁺ early TEM signature), and effector/resident memory CD8 T cells
331 (enrichment of prostate CD8 effector T cell signature, expression of CD103, GzmB,
332 TOX2; Figure 6B). These subsets were not significantly altered by ADT or ADT + anti-
333 CTLA4-NF. To further interrogate tumor-infiltrating CD8 T cell phenotypes by CyTOF,
334 we used semi-supervised FlowSOM clustering to define eight CD8 T cell subclusters
335 (Figure 6D). While these clusters did not map precisely onto the three cluster solution in
336 the scRNAseq data, we did observe clusters that most closely matched the effector
337 memory (Tc.4; CD45RA⁻CD45RO⁺CD27⁺HLA-DR⁺PD-1^{mid}) phenotype and cells that
338 matched the effector/resident memory (Tc.6; CD45RO⁻HLA-DR⁺CTLA-4⁺TIGIT⁺GzmB⁺)
339 phenotype that mirrored non-significant trends in the scRNAseq data after anti-CTLA4-
340 NF (Extended Data Fig 6C-D). Notably, we also observed a cluster with clear
341 enrichment in a subset of patients receiving ADT + anti-CTLA4-NF defined by 4-1BB
342 and CD39 (Figure 5E-G), markers that are associated with recently primed and tumor-
343 specific T cells^{35,36}. We found the dual 4-1BB⁺CD39⁺ phenotype to also define a distinct
344 subset of CD4⁺FoxP3⁻ conventional CD4 T cells (Tconv) that were uniquely present in a

345 subset of patients receiving ADT + anti-CTLA4-NF (Figure 5H-K, Extended Data 6E-F).
346 These data suggest anti-CTLA4-NF may enhance priming of tumor-specific T cell
347 populations, either in concert with or independent of Treg depletion. To test whether this
348 effect requires Fc γ R interactions, we returned to our murine model where we profiled
349 effects of anti-CTLA4 (D) versus anti-CTLA4 (ND) in combination with ADT. We
350 observed a distinct cluster of 4-1BB⁺CD39⁺ CD8 T cells in Myc-CaP tumors that were
351 uniquely induced by ADT + anti-CTLA4 (D) and were absent in ADT-only and ADT +
352 anti-CTLA4 (ND) groups (Figure 5L-O, Extended Data Fig 6G-I), indicating Fc γ R
353 engagement is required for induction of the 4-1BB⁺CD39⁺ CD8 T cell phenotype under
354 anti-CTLA4 therapy. Supporting our hypothesis that these cells represent a recently
355 primed population, we found a significant increase in CD8 and CD4 Tconv cells bearing
356 phenotypic markers of recent priming (CD44⁺Ki67⁺) in tumor draining LNs (tdLNs) in
357 mice receiving anti-CTLA4 (D) relative to anti-CTLA4 (ND) or ADT alone (Figure 5P-R,
358 Extended Data Fig 6J). This was not associated with Treg depletion in the tdLNs, but
359 rather an increase in Treg frequency in the tdLNs as has been previously shown in the
360 context of anti-CTLA4 therapeutics³⁷ ($p < 0.0001$; Extended Data Figure 6K). These
361 findings support an additional putative mechanism of action of Fc engineered anti-
362 CTLA4-NF antibodies, potentially distinct from Treg depletion, involving enhanced
363 priming of tumor-specific CD8 and/or non-Treg CD4 Tconv cells.

364 **Discussion**

365

366 This study evaluated a novel next-generation non-fucosylated anti-CTLA4 antibody
367 (BMS-986218) engineered to enhance ADCC in combination with ADT versus ADT
368 alone prior to surgery in men with high-risk localized PCa. We demonstrated that anti-
369 CTLA4-NF shows promising signs of biological activity to counteract ADT-induced Treg
370 expansion in patients, consistent with its proposed mechanism of action, and promotes
371 successful immune priming in PCa. Anti-CTLA4-NF treatment also demonstrated a
372 tolerable safety profile in the pre-surgical setting and potential clinical activity with a
373 lower-than-expected rate of recurrence.

374 To determine potential mechanisms underlying the immunological effects of anti-
375 CTLA4-NF on the TME, we utilized multiple analytic methods to interrogate changes in
376 immune phenotypes at the single-cell level on prostatectomy specimens. These studies
377 revealed both expected and novel associations with response to therapy. We showed
378 for the first time in patients that anti-CTLA4-NF elicits measurable TI-Treg depletion
379 through engagement of the activating FcγR CD16a on tumor macrophages and that the
380 depth of Treg depletion correlates with clinical outcome. Our findings thus support the
381 mechanism established in pre-clinical models but for which limited clinical evidence
382 currently exists^{16,29}. These findings also support the hypothesis that first-generation anti-
383 CTLA4 antibodies ipilimumab and tremelimumab fail to deplete TI-Tregs in humans due
384 to inefficient engagement of CD16a on TAMs. A possible explanation for this
385 phenomenon is that non-engineered anti-CTLA4 IgG1 antibodies preferentially engage
386 the inhibitory FcγR *FCGR2B/CD32b* on myeloid cells, preventing TI-Treg-directed
387 ADCC/P³⁸. Complicating this mechanism is our observation that inhibitory *FCGR2B* and

388 activating *FCGR3A* receptors are highly co-expressed on tumor associated
389 macrophages. Additional studies are warranted to understand how co-expression
390 patterns of *FCGR3A* and *FCGR2B* on TAMs influences efficiency of Treg depletion by
391 Fc-engineered antibodies targeting CTLA-4. An alternative mechanism supported by
392 our data is that tumors with low baseline frequencies of *FCGR3A/CD16a*⁺ TAMs – or
393 physical segregation of these macrophages from TI-Tregs – may fail to respond to anti-
394 CTLA4-NF. A positive role for *FCGR3A/CD16a*⁺ TAMs in the context of anti-CTLA4-NF
395 is notable, as *FCGR3A/CD16a*⁺ TAMs are generally enriched for the
396 immunosuppressive, M2-like phenotype (e.g. TREM2⁺ and CD206⁺ TAMs in our study)
397 that plays a negative prognostic role in many cancers²². However, the role of these
398 TAMs may vary in distinct therapeutic contexts. Recent data suggest M2-like TAMs may
399 in fact be necessary to organize antitumor immune responses³⁹, which together with our
400 findings challenges the narrative that M2-like TAMs are universally antagonistic to
401 cancer immunotherapies. In either case, pre-clinical studies suggest anti-CTLA4-
402 mediated FcγR engagement on tumor macrophages can elicit pro-inflammatory
403 macrophage skewing⁴⁰. Therefore, Fc-engineered anti-CTLA4 antibodies may deliver a
404 broadly applicable, and possibly synergistic, dual benefit of TI-Treg depletion and M2-
405 to-M1 macrophage skewing that may be effective in overcoming the
406 immunosuppressive microenvironment of many tumor types that do not respond to ICB.

407 Although anti-CTLA4-NF decreased TI-Treg frequency in PCa patients, TI-Treg
408 depletion was not complete. Residual Tregs in tumors following treatment with anti-
409 CTLA4-NF appear to exhibit a highly activated phenotype. While our current studies
410 were not able to confirm whether these Tregs were functionally immunosuppressive,

411 these findings indicate a potential limitation of TI-Treg depleting therapies that target a
412 single coinhibitory receptor such as CTLA4. We hypothesize that TI-Tregs undergoing
413 blockade of CTLA4 without experiencing ADCC/P (whether through engagement of
414 *FCGR2B* on proximal TAMs or spatial segregation from ADCC/P effectors) become
415 activated as a result of less coinhibitory receptor activity, as has been observed in mice
416 receiving anti-CTLA4 or in context of anti-PD1 blockade^{37,41}. Notably, we found these
417 Tregs to be enriched in other potentially targetable surface proteins, such as CCR8,
418 CD25, CD39, and 4-1BB. Fc competent and glycoengineered antibodies targeting
419 CCR8 are currently in clinical development^{42,43}. Thus, co-delivery of glycoengineered
420 antibodies targeting CTLA-4 and CCR8 may be additive or synergistic, given the
421 potential capacity for anti-CCR8 to deplete TI-Tregs remaining following anti-CTLA4,
422 and that anti-CTLA4 elicits enhanced T cell priming and myeloid activation. Recent
423 studies also suggest CD4 Tconv in tumors depleted of TI-Tregs upregulate CCR8 and
424 become functionally immunosuppressive⁴⁴. These studies warrant additional basic and
425 clinical studies of glycoengineered antibodies targeting CTLA4 and CCR8 in prostate or
426 other cancers.

427 In addition to Treg depletion, we found that our glycoengineered anti-CTLA4
428 antibody enhanced T cell priming, potentially by increasing interactions between
429 CTLA4+ effector T cells and FcγR+ dendritic cells. High tumor DC frequencies in our
430 data were significantly associated with lack of disease recurrence in patients receiving
431 ADT + anti-CTLA4-NF. In addition, only patients treated with anti-CTLA4-NF elicited the
432 distinct CD39⁺41BB⁺ phenotype in tumor-infiltrating CD8 and CD4 T cells, mirroring
433 established phenotypes for tumor-specific T cells (CD39⁺CD103⁺³⁵) and recently primed

434 tumor-specific cells (41BB⁺). Our pre-clinical studies in the murine syngeneic MycCaP
435 model were in striking agreement with these clinical data, and prior *in vitro* work with
436 human T cells and DCs in context of bacterial superantigen-mediated stimulation
437 suggest FcγR engagement on APCs is required for enhanced priming activity of
438 antibodies targeting CTLA-4, independent of Treg depletion⁴⁵. Our pre-clinical findings
439 that FcγR-engaging – but not FcγR-silenced – anti-CTLA-4 antibodies elicit a significant
440 phenotypic shift in tumor DCs suggests a bi-directional effect on both T cells and DCs,
441 reminiscent of observed inflammatory polarization of macrophages post-anti-CTLA-4 in
442 other murine models⁴⁰. Nevertheless, increasing evidence indicates spatial co-
443 localization of effector CD8 and CD4 T cells with DCs in tumors (termed immune
444 “triads,” “hubs” or “networks”^{46,47}) is critical for productive antitumor immune responses.
445 Further investigation is warranted to determine whether Fc-enhanced antibodies
446 targeting CTLA-4 or other immune checkpoints can facilitate accumulation of these
447 specialized immune clusters in human tumors, and whether this is an essential
448 underlying mechanism of action of these therapeutics.

449 One limitation of our study was the relatively small sample size making
450 interpretation of clinical activity of ADT + anti-CTLA4-NF challenging. Although we
451 observed a lower rate of recurrence following surgery than would be expected based on
452 established risk nomograms, both ADT alone and ADT plus anti-CTLA4-NF
453 demonstrated favorable outcomes. A second limitation was that our study was not
454 designed with sufficient power to compare outcome differences between the treatment
455 arms. In terms of profiling data; given that our CyTOF and scRNAseq was performed on
456 freshly collected specimens, all comparisons were made between treatment groups as

457 opposed to matched pre- and post-treatment tissue, which was not available. However,
458 the arms were relatively well balanced and previous data suggests comparisons
459 between pre-treatment biopsies and surgical resection tissue may be confounded when
460 assessing the immune TME⁴⁸. Clinically, it is notable that development of BMS-986218
461 has been discontinued (NCT03110107), however, several related second-generation
462 depleting anti-CTLA4 antibody agents (botensilimab/AGEN1181, ONC-392, ADG216)
463 are in clinical development. Of note, recent findings from Chand *et al.* indicate
464 botensilimab, an Fc-enhanced DLE-mutated anti-CTLA4-hIgG1 antibody, depletes Tl-
465 Tregs in an FcγR-dependent fashion across cancer types and potentially modulates
466 DCs, closely mirroring our pre-clinical and clinical findings with BMS-986218 in PCa¹².

467 Unfortunately, ICB has been ineffective for the vast majority of patients with
468 prostate cancer. However, a more nuanced appreciation of key mechanisms of immune
469 tolerance in prostate cancer and how these evolve with disease progression and vary
470 by site of disease is allowing for the development of novel therapeutic approaches. Our
471 study builds on prior work demonstrating that ADT rapidly elicits a particularly robust
472 immune response in the neoadjuvant setting but is limited by adaptive Treg
473 resistance¹¹. In murine prostate cancer models ADT combined with Treg depletion
474 results in durable tumor control supporting the development of novel Treg depletion
475 strategies in patients¹⁰. Prior studies have evaluated ipilimumab prior to surgery in
476 prostate cancer but have demonstrated limited efficacy and significant toxicity⁴⁹ (also
477 see NCT02020070).

478 Although traditional drug development has focused on heavily pre-treated
479 advanced disease first to establish clinical efficacy before moving to earlier disease

480 settings, this approach has several shortcomings in the context of immunotherapy. In
481 particular the neoadjuvant setting may be uniquely effective given the abundance of
482 tumor antigens, presence of tumor-draining lymph nodes to allow for tumor antigen
483 cross-presentation and T cell priming, and overall more permissive immune tumor
484 microenvironment. Furthermore, the neoadjuvant setting opens a unique window of
485 opportunity to rapidly assess biological mechanisms of response versus resistance that
486 are challenging in other disease settings. In the NeoRED-P study, we establish the
487 feasibility of such an approach using a novel agent that has not previously been tested
488 in prostate cancer.

489 In conclusion, we demonstrate the safety and feasibility of anti-CTLA4-NF (BMS-
490 986218) in combination with ADT prior to surgery in men with high-risk localized
491 prostate cancer. Our robust immune profiling studies provide first-in-human evidence of
492 TI-Treg depletion by glycoengineered antibodies targeting CTLA-4. In combination with
493 pre-clinical modeling these findings support both canonical and novel mechanisms
494 underlying activity of ADCC/P-competent anti-CTLA4. Our study also identifies
495 immunological correlates of clinical response to ADT + anti-CTLA4-NF, supporting a
496 potential role for immunotherapy targeting CTLA-4 in patients with prostate cancer.

497

Tables

Table 1. Patient Baseline Demographics and Disease Characteristics

Characteristic	ADT N=10 ¹	ADT + αCTLA-4-NF N=14 ¹
Age		
Median (Range)	66.0 (52.0, 72.0)	65.5 (52.0, 77.0)
Race, n (%)		
White	6 (60%)	9 (64%)
Black	2 (20%)	2 (14%)
Asian	1 (10%)	0 (0%)
Other	1 (10%)	3 (21%)
Ethnicity, n (%)		
Not Hispanic	7 (70%)	12 (86%)
Hispanic	3 (30%)	2 (14%)
PSA²		
Median (Range)	18.44 (2.37, 94.40)	9.08 (4.57, 364.70)
Testosterone		
Median (Range)	420.30 (153.90, 553.30)	399.50 (273.80, 783.30)
Grade group, n (%)		
3	5 (50%)	2 (14%)
4	3 (30%)	5 (36%)
5	2 (20%)	7 (50%)
T stage, n (%)		
T2	5 (50%)	4 (29%)
T3a	2 (20%)	5 (36%)
T3b	3 (30%)	5 (36%)
Nodal involvement, n (%)	2 (20%)	3 (21%)
Surgical margin involvement, n (%)	3 (30%)	3 (21%)
2-year recurrence-free probability		
Median (Range)	69.50 (8.00, 88.00)	55.00 (4.00, 82.00)
VHR, n (%)³	8 (80%)	12 (86%)

¹ Median (Range) for continuous variables; N (%) for categorical variables

² Prostate-specific antigen (PSA), ng/mL

³ Very high-risk (VHR) group defined by National Comprehensive Cancer Network (NCCN) criteria as Gleason ≥8 or PSA >20 ng/ml or clinical T3 stage or higher

Table 2. Treatment-related adverse events

Treatment-related adverse events (TRAEs) [†]	ADT N = 10		ADT + αCTLA-4-NF N = 14	
	All grades	Grade ≥3	All grades	Grade ≥3
Any treatment-related adverse event (TRAE)	8 (80)	—	10 (71)	1 (7.1)
Gastrointestinal disorders	—	—	3 (21)	—
<i>Colitis</i>	—	—	1 (7.1)	—
<i>Diarrhea</i>	—	—	1 (7.1)	—
<i>Elevated transaminases</i>	—	—	1 (7.1)	—
General disorders and administration site conditions	7 (70)	—	8 (57)	—
<i>Chills</i>	1 (10)	—	—	—
<i>Fatigue</i>	—	—	4 (29)	—
<i>Hot flashes</i>	5 (50)	—	6 (43)	—
<i>Injection site reaction</i>	6 (60)	—	7 (50)	—
Investigations	—	—	—	1 (7.1)
<i>Lipase increased</i>	—	—	—	1 (7.1)
Musculoskeletal and connective tissue disorders	—	—	1 (7.1)	—
<i>Bone pain</i>	—	—	1 (7.1)	—
Nervous system disorders	—	—	1 (7.1)	—
<i>Headache</i>	—	—	1 (7.1)	—
Reproductive system disorders	2 (20)	—	—	—
<i>Erectile dysfunction</i>	2 (20)	—	—	—
Skin and subcutaneous tissue disorders	—	—	1 (7.1)	—
<i>Pruritus</i>	—	—	1 (7.1)	—

[†] Treatment-related adverse events (TRAEs) graded according to NCI CTCAE v5.0

Table 3. Study Outcomes

Outcome	N	ADT N=10 [†]	ADT + αCTLA-4-NF N=14 [†]
PSA response rate²	22	3 (33%)	7 (54%)
Undetectable PSA at 12 months	23	8 (80%)	10 (77%)
Time recurrence-free (months)	23		
<i>Median (Range)</i>		23.8 (2.2, 25.3)	22.9 (3.2, 26.6)
Overall recurrence	24	2 (20%)	4 (29%)

[†] Median (Range) for continuous variables; N (%) for categorical variables

² PSA response rate defined as >50% decrease in PSA prior to prostatectomy

Figure Legends

498 **Figure 1: NeoRED-P trial design and clinical outcomes. (A)** Schematic of NeoRED-
499 P clinical trial design. **(B)** NeoRED-P trial consort diagram. **(C)** Kaplan-Meier curve of
500 PSA recurrence-free survival in patients treated with neoadjuvant ADT. **(D)** Kaplan-
501 Meier curve of PSA recurrence-free survival in patients treated with neoadjuvant ADT +
502 anti-CTLA4-NF. Predicted median 2-year RFS in **(C)** and **(D)** were calculated from the
503 Memorial Sloan Kettering Cancer Center Post-Radical Prostatectomy Prediction risk
504 nomogram. **(E)**. Percent change in serum PSA from pre-treatment to time of surgery in
505 ADT arm patients. Dotted line denotes 50% decline in PSA (PSA50). **(F)** Percent
506 change in serum PSA from pre-treatment to time of surgery in ADT + anti-CTLA4-NF
507 arm patients.

508

509

510 **Figure 2: Multi-omic single cell analysis of Treg depletion by ADT + anti-CTLA4-**
511 **NF. (A)** Schematic of immune correlates performed. **(B)** Summary of data collection and
512 QC passing at a per-patient level for CyTOF, scRNAseq, and immunofluorescence
513 datasets. Patients are additionally annotated according to presence or absence of PSA
514 recurrence within 2 years post-surgery. **(C)** Representative images from whole-slide
515 immunofluorescence data for CD4 and FoxP3 with DAPI nuclear staining. Inset grey
516 box shows a representative CD4⁺FoxP3⁺ cell at 2.5x magnification relative to the
517 original image. Scale bar = 40µm. **(D)** Violin plot representing Treg density as measured
518 by Treg cell number per mm² between NeoRED-P treatment groups and untreated
519 controls in the immunofluorescence dataset. **(E)** UMAP plot of single cell RNAseq data

520 from all patients, clustered using the PICSES analytical pipeline. **(F)** Bubble plot of
521 representative gene expression for each cluster identified in **(E)**. **(G)** Supervised UMAP
522 plot of CyTOF data from all patients, clustered using FlowSOM. **(H)** Heatmap of lineage-
523 defining protein expression across all clusters. Data represents geometric MFI for each
524 marker normalized to the minimum and maximum values across all clusters. **(I)** UMAP
525 plot representing subclustering of the scRNAseq T/NK cluster shown in **(E)**. **(J)**
526 Visualization of per-cell normalized enrichment scores for a published Treg gene set
527 across all T/NK cells in the scRNAseq dataset. **(K)** Bubble plot of inferred protein
528 activity for manually selected Treg-related proteins across all T/NK subclusters as
529 calculated by VIPER. **(L)** Violin plot representing Treg frequencies as a percent of total
530 cells between NeoRED-P treatment groups and untreated controls in the scRNAseq
531 data. **(M)** Overlay of FlowSOM-derived Treg and CD4 Tconv clusters in the CyTOF data
532 on bi-axial plots representing canonical Treg phenotypes. **(N)** Heatmap of all Treg-
533 relevant phenotypic marker expression in the CyTOF panel, normalized as described in
534 **(H)**. Markers with universally high or low expression were scaled according to the
535 minimum and maximum of all FlowSOM clusters. **(O)** Violin plot representing Treg
536 frequencies as a percent of total cells between NeoRED-P treatment groups and
537 untreated controls in the CyTOF data. All statistical tests in this figure utilized Student's t
538 test.

539

540 **Figure 3: Phenotypic analysis of TI-Tregs and association with clinical outcomes.**

541 **(A)** PaCMAP plot representing FlowSOM-derived Treg clusters in the CyTOF data. Data
542 presents 17,757 total cells across 25 patients with evaluable data. Clusters were

543 manually annotated according to expression of relevant protein markers as visualized in
544 **(B)** as colorimetric expression maps of selected markers overlaid on the parent
545 PaCMAP plot, or **(C)** heatmap expression of all relevant markers across all clusters.
546 Data represents geometric MFI for each marker normalized to the minimum and
547 maximum values across all clusters. Markers with universally high or low expression
548 were scaled according to the minimum and maximum of all CD45⁺ FlowSOM clusters.
549 **(D)** Density plots representing Treg cell location on the PaCMAP plot in **(A)** iterated by
550 treatment group. **(E)** Stacked box plot quantifying relative frequencies of all Treg
551 FlowSOM-derived clusters as a percent of Tregs the PaCMAP plot in **(A)** iterated by
552 treatment group. **(F)** Bubble plot representing relative expression of phenotypic markers
553 in Tregs from ADT + anti-CTLA4-NF group versus Tregs in the ADT only group, as
554 calculated by log₂ transformed ratio of average geometric MFI of each marker on Tregs
555 from ADT + anti-CTLA4-NF versus ADT groups. Bubble size represents relative gMFI,
556 while color intensity represents percent expression of indicated markers across all
557 Tregs in the dataset. Red color indicates higher relative gMFI in Tregs from patients
558 treated with ADT + anti-CTLA4-NF, while blue color indicates higher relative gMFI in
559 patients treated with ADT only. **(G)** Violin plot representing frequency of Tregs at time of
560 surgery in the scRNAseq dataset stratified by 2-year PSA recurrence status. Student's
561 t-test was performed to evaluate statistical significance. **(H)** Kaplan-Meier curve
562 representing time-to-PSA recurrence in ADT + anti-CTLA4-NF treated patients stratified
563 by Treg frequency (in scRNAseq data). Log-rank test was performed to evaluate
564 statistical significance.
565

566 **Figure 4: Myeloid correlates of Treg depletion and response to anti-CTLA4-NF. (A)**
567 UMAP plot representing subclustering of myeloid cells in the scRNAseq dataset utilizing
568 the PISCES pipeline. **(B)** Visualization of representative gene expression overlaid on
569 the parent UMAP plot to validate cluster annotations. **(C)** Bubble plot validating
570 expression of additional cluster defining genes. **(D)** Visualization of VIPER-inferred
571 protein activity of select Fcγ receptors across myeloid clusters in UMAP space. **(E)**
572 Violin plot of *FCGR3A/CD16a* inferred protein activity on a per cell level stratified by
573 myeloid cluster. **(F)** Correlation between Treg frequency and average inferred protein
574 activity of *FCGR3A/CD16a* across all myeloid cells on a per patient basis, stratified by
575 treatment group. **(G)** Correlation between Treg frequency and average inferred protein
576 activity of *FCGR3A/CD16a* across TREM2⁺ TAM cluster cells on a per patient basis,
577 stratified by treatment group. Pearson correlations were utilized to evaluate statistical
578 significance of correlations. **(H)** Violin plot of myeloid cluster frequencies as a percent of
579 myeloid cells stratified by treatment group. **(I)** Violin plot of myeloid cluster frequencies
580 as percent of myeloid cells stratified by patient 2-year PSA recurrence status. Student's
581 t-test was utilized to test statistical significance. **(J)** Kaplan-Meier curve representing
582 time-to-PSA recurrence in patients stratified by dendritic cell frequency. Log-rank test
583 was performed to evaluate statistical significance. **(K)** Schematic of pre-clinical
584 validation experiment in the MycCaP model. **(L)** Percent change in tumor volume
585 relative to baseline volume prior to ADT stratified by treatment group. Average values
586 are represented by solid lines and standard deviations are represented by shaded
587 areas. **(M)** Kaplan-Meier curve representing survival of mice shown in **(K-L)**. Log-rank
588 (Mantel-Cox) test was used to evaluate statistical significance. **(N)** Top: Supervised

589 UMAP of live CD45⁺ cells from MycCaP tumors harvested following therapy as denoted
590 in **(K-M)**. Semi-supervised clustering was performed using FlowSOM and clusters were
591 manually annotated according to expression of lineage-defining markers. Bottom:
592 Heatmap of lineage-defining markers across all clusters. Data represents geometric MFI
593 for each marker normalized to the minimum and maximum values across all clusters.
594 **(O)** Frequency of TI-Tregs and cDCs as percent of all live CD45⁺ cells, stratified by
595 treatment group. **(P)** PaCMAP representing FlowSOM-derived cDC clusters. Clusters
596 were manually annotated according to expression of canonical marker proteins,
597 representative markers shown at right. Below: Pseudocolor representation of cDC
598 phenotypes in PaCMAP space stratified by treatment group. **(Q)** Violin plot representing
599 frequency of PD-L2⁺ DCs as percent of all live CD45⁺ events stratified by treatment
600 group. Student's t-test was used to assess statistical significance. All murine data
601 shown is representative of two independent experiments of 5-10 mice per group each
602 for survival and immune profiling studies.

603

604 **Figure 5: Phenotypic modulation and induced priming of CD8 T cells by anti-**
605 **CTLA4-NF. (A)** UMAP plot representing subclustering of CD8 T cells in the scRNAseq
606 data utilizing the PICSES pipeline. **(B)** Visualization of representative gene expression
607 signatures or inferred activity of indicated proteins overlaid on the parent UMAP plot to
608 validate cluster annotations **(C)** Violin plot of CD8 T cell cluster frequencies as a percent
609 of CD8 T cells stratified by treatment group. **(D)** PaCMAP plot of NeoRED-P patient
610 tumor-infiltrating CD8 T cells by CyTOF. Clusters were derived from FlowSOM. **(E)**
611 Pseudocolor density plots of CD8 T cells in PaCMAP space stratified by treatment

612 group. **(F)** Expression of CD39 and 4-1BB by geometric MFI on CD8 T cells as
613 represented by color mapping on PaCMAP plot. **(G)** Violin plot representing frequency
614 of manually gated CD39⁺4-1BB⁺ CD8 T cells as a percentage of all CD8 T cells
615 stratified by treatment group. **(H)** PaCMAP plot of NeoRED-P patient tumor-infiltrating
616 CD4⁺ FoxP3⁻ Tconv cells by CyTOF. Clusters were derived from FlowSOM. **(I)**
617 Pseudocolor density plots of CD4 Tconv cells in PaCMAP space stratified by treatment
618 group. **(J)** Expression of CD39 and 4-1BB by geometric MFI on CD4 Tconv as
619 represented by color mapping on PaCMAP plot. **(K)** Violin plot representing frequency
620 of manually gated CD39⁺4-1BB⁺ CD4 Tconv cells as a percentage of all CD8 T cells
621 stratified by treatment group. **(L)** PaCMAP plot of MycCaP-infiltrating CD8 T cells by 45-
622 parameter flow cytometry in response to ADT, ADT + anti-CTLA4 (ND), or ADT + anti-
623 CTLA4 (D). Clusters were derived from FlowSOM. **(M)** Pseudocolor density plots of
624 CD8 T cells in PaCMAP space stratified by treatment group. **(N)** Expression of CD39
625 and 4-1BB by geometric MFI on CD8 T cells as represented by color mapping on
626 PaCMAP plot. **(O)** Violin plot representing frequency of manually gated CD39⁺4-1BB⁺
627 CD8 T cells as a percentage of all CD8 T cells stratified by treatment group. **(P)** Biaxial
628 plots representing expression of CD44 and Ki67 on CD8 T cells in tumor draining lymph
629 nodes of mice shown in **(L-O)**. **(Q)** Biaxial plots representing expression of CD44 and
630 Ki67 on CD4⁺FoxP3⁻ Tconv cells in tumor draining lymph nodes of mice shown in **(L-O)**.
631 **(R)** Violin plots representing frequencies of CD44⁺Ki67⁺ CD8 and CD4 Tconv cells as a
632 percentage of parent populations stratified by treatment group. Student's t-test was
633 used to assess statistical significance. All murine data shown is representative of two

634 independent experiments of 5-10 mice per group each for survival and immune profiling

635 studies.

636

637 **Methods**

638

639 **Patients**

640 Key eligibility criteria included histologically confirmed adenocarcinoma of the prostate
641 (clinical stage T1c-T3b, N0, M0) with no detectable metastatic involvement of lymph
642 nodes, bone, or visceral organs and high-risk disease as defined by central pathologic
643 review of at least two biopsy cores with Gleason sums of $\geq 4+3$. Patients were required
644 to demonstrate adequate bone marrow, hepatic, and renal function. Prior exposure to
645 radiation therapy, chemotherapy, immunotherapy, biologic therapy, or concomitant
646 treatment with hormonal therapy and/or systemic corticosteroids (with the exception of
647 short courses < 5 days 7 days or more prior to treatment initiation) was not allowed. See
648 full trial protocol in Supplementary Information for additional detail.

649 **Clinical Trial Regulatory Oversight and Approval**

650 This trial was approved and all amendments reviewed by the Columbia University
651 Institutional Review Board (IRB) under the protocol number AAAS3560. The trial was
652 registered with ClinicalTrials.gov on March 6, 2020, with the ClinicalTrials.gov ID
653 NCT04301414. All patients provided informed consent prior to enrollment in the study.

654 **Clinical Trial Design**

655 This was a single-center, randomized, two-arm, open label pilot study conducted at
656 Columbia University Irving Medical Center to evaluate the safety, feasibility, and
657 immunogenicity of neoadjuvant degarelix (ADT) or BMS-986218 (anti-CTLA4-NF) plus
658 ADT prior to radical prostatectomy in men with high-risk localized prostate cancer.²⁴
659 patients were enrolled in the study. The first 4 patients were assigned to receive ADT +
660 anti-CTLA4-NF as a safety lead-in. Thereafter, 10 patients each were randomized to the
661 two treatment arms. In the ADT-only arm, men received 240 mg degarelix acetate
662 subcutaneously two weeks prior to surgery. In the ADT + anti-CTLA4-NF arm, men
663 received 20 mg BMS-986218 intravenously on day 1 and day 15, and 240 mg degarelix
664 acetate subcutaneously on day 8, starting 3 weeks prior to prostatectomy (Figure 1A).

665 **Clinical Trial Endpoints and Assessments**

666 The primary objective was to characterize safety, tolerability, and feasibility of ADT with
667 or without anti-CTLA4-NF in the neoadjuvant setting. The secondary objectives
668 included: (i) evaluation an immune response consistent with the proposed mechanism
669 of action of anti-CTLA4-NF, specifically the effect on intratumoral Treg density and
670 CD8:Treg ratio, (ii) estimation of the pathologic complete response rate following
671 neoadjuvant anti-CTLA4-NF plus ADT as compared to ADT alone, (iii) estimation of the
672 PSA50 response rate and rate of undetectable PSA at 12 months following neoadjuvant
673 anti-CTLA4-NF plus ADT as compared to ADT alone, and (iv) estimation of the rate of
674 post-surgical PSA recurrence within two years of completing therapy between patients
675 receiving ADT alone versus ADT plus anti-CTLA4-NF.

676 Serum PSA and testosterone levels were measured on all patients prior to therapy
677 initiation and at time of surgery. Thereafter, serum PSA and testosterone was measured
678 on all patients every 3 (± 1) months during the first post-operative year and every 6 (± 2)
679 months during the second and third post-operative years. Adverse events were
680 monitored during the course of therapy and until at least two years post-surgery and
681 registered according to CTCAE version 5.0. Adverse events were deemed associated
682 or not associated with ADT and/or anti-CTLA4-NF according to the treating physician.
683 Peripheral blood was drawn weekly during the course of treatment and at follow-up
684 visits after surgery. Tumor samples from prostatectomy specimens were collected at
685 time of surgery; fresh tissue was collected and processed as described below, and
686 archival formal-fixed paraffin-embedded (FFPE) tissues were obtained for indicated
687 correlative studies.

688 **Tumor Sample Collection & Processing**

689 Following radical prostatectomy, surgical tissues were grossed and sectioned by
690 pathologists at Columbia University Irving Medical Center. Up to 1 gram of tumor tissue
691 was collected in Miltenyi MACS Tissue Storage Solution on wet ice, massed, washed
692 with PBS, then diced with microdissection scissors to 1-2mm pieces in a 5mL
693 Eppendorf tube. Tissue pieces were transferred into a Miltenyi C tube (0.5g per tube) in
694 serum free RPMI, then enzymes H, R, and A were added according to the Miltenyi
695 Human Tumor Dissociation Kit protocol. Tumors were digested on a gentleMACS

696 Octodissociator under program 37_multi_A_01. Once finished, RPMI supplemented
697 with 5% FBS (R5 media) was added to quench digest enzymes, then suspensions were
698 filtered (70um) into a 15mL conical tube and spun at 400xg for 5 minutes at 4° C.
699 Pellets were RBC lysed by resuspension in Miltenyi 1x ACK buffer for 5 minutes at RT,
700 followed by centrifugation at 300xg for 5 min at 4° C. Pellets were washed with R5,
701 filtered, and pelleted. Cell numbers were then quantified on a Countess II automated
702 cell counter, then samples were split for downstream analysis by CyTOF and single cell
703 RNA sequencing.

704 **Tumor Whole Exome Sequencing**

705 Baseline germline mutation testing was performed at trial screening using the Invitae
706 Common Hereditary Cancers Panel (48 genes) or the Invitae Multi-Cancer Panel (70
707 genes). Archival formalin-fixed, paraffin-embedded (FFPE) tumor specimens with >30-
708 40% tumor content were sectioned at 5uM by the Herbert Irving Comprehensive Cancer
709 Center's (HICCC) Molecular Pathology Shared Resource (MPSR). Hematoxylin and
710 eosin (H&E) slides were reviewed and tumor area marked by a board-certified
711 pathologist. Tissue sections were submitted for mutational profiling to Columbia
712 University Irving Medical Center's Laboratory of Personalized Genomic Medicine, a
713 CAP-accredited and CLIA-certified clinical genomics laboratory. Tissue was prepared
714 for sequencing as previously described⁵⁰.

715 Targeted next-generation sequencing of tumor DNA and cDNA was performed using
716 the Columbia Combined Cancer Panel (CCCP), a New York State Department of
717 Health-certified panel, covering 467 cancer-related genes Raw sequencing data were
718 mapped to the human reference genome (GRCh37, hg19), and analyzed for single
719 nucleotide variants, small insertions and deletions, copy number alterations, gene
720 rearrangements and fusions, tumor mutation burden, and microsatellite instability using
721 validated clinical pipelines. Identified genomic alterations were reviewed and interpreted
722 for pathogenicity and clinical significance by a board-certified molecular pathologist. See
723 supplementary Information for genes covered in all genomic testing panels and panel-
724 specific methodologies.

725

726 **Mass Cytometry**

727 Cell pellets were resuspended in R5 supplemented with Rh103 viability stain (1:500) in
728 a 1.5mL protein lo-bind tube and incubated 15 min at 37° C. Cells were pelleted,
729 washed once with R5 media, then resuspended in 49ul Cell Staining Buffer (CSB;
730 Fluidigm) followed by addition of 1ul Fc Block (TruStain FcX; BioLegend). Samples
731 were mixed and incubated for 5-10 minutes on ice. Separate surface and intracellular
732 antibody cocktails were pre-mixed and stored at -80° C; during the Fc Block incubation
733 cocktails were thawed on ice, the surface mix was spun through a PVDF centrifuge filter
734 for 3 min at 1200rpm, then 50ul surface mix was added to the cell suspension for a final
735 volume of 100ul. Surface staining was conducted on ice for 30 minutes, then cells were
736 washed twice with 1mL CSB. Cells were fixed by resuspending in 500ul FoxP3
737 Fixation/Permeabilization buffer (eBioscience) and incubating at RT for 30 minutes.
738 Fixative was washed out with two successive washing steps with 1mL 1X Perm Wash.
739 For intracellular staining, cells were resuspended in 49ul 1X PW + 1ul heparin on ice.
740 Intracellular cocktails were diluted to 50ul with 1X PW and were spun through a PVDF
741 membrane prior to addition to the cell solution for a final staining volume of 100ul. Cell
742 staining was conducted on ice for 30 minutes, followed by two successive washes with
743 1mL 1X PW. Fully stained cells were fixed in 400ul FixIR solution (2.4% PFA + 0.25 nM
744 Ir-191/193) at room temperature for 30 minutes. Samples were washed with 600ul CSB
745 and spun for 4 min at 600 xg, and washed again with 1mL CSB. Samples were either
746 resuspended in CSB and held at 4° C for a maximum of 72 hours before being acquired
747 on a CyTOF Helios at the Columbia University Human Immune Monitoring Core
748 (HIMC), or frozen at -80° C in FBS + 10% DMSO before being thawed and acquired on
749 a CyTOF Helios at either the Columbia University HIMC or the Mayo Clinic Immune
750 Monitoring Core (IMC). All samples were acquired with, and data was normalized using
751 spiked in four-element EQ Calibration Beads (Fluidigm/Standard BioTools) for
752 longitudinal and cross-platform standardization.

753 **Single Cell RNA Sequencing and Analysis**

754 Cells were processed for scRNAseq using the 10X Chromium 3' v2 Library and Gel
755 Bead Kit (10x Genomics) according to manufacturer's instructions at the Columbia

756 University HIMC and as described previously²². ScRNASeq data were processed with
757 Cell Ranger software at the Columbia University Single Cell Analysis Core. Illumina
758 base call files were converted to FASTQ files with the command “cellranger mkfastq.”
759 Expression data were processed with “cellranger count” on the pre-built human
760 reference set of 30,727 genes. Cell Ranger performed default filtering for quality control.
761 The Seurat package was used for quality control filtering of cells, excluding those with
762 fewer than 10% mitochondrial RNA content, more than 1,500 unique UMI counts, and
763 fewer than 15,000 unique UMI counts. Pooled distribution across all samples of UMI
764 counts, unique gene counts, and percentage of mitochondrial DNA after QC-filtering is
765 shown in Extended Data Figure 3A.

766 *Gene Expression Clustering and Initial Cell Type Inference* | Combined and normalized
767 gene expression matrix was visualized by UMAP projection and unsupervised clustering
768 was performed using the Louvain algorithm applied to top50 principal components of
769 the full data matrix, with optimal clustering resolution determined by bootstrapped
770 silhouette score optimization, as described in prior work²². Broad cell types were
771 inferred by SingleR with blueprint-ENCODE reference of sorted cell types, with each
772 cluster consensus-labelled by majority-inferred cell type²⁴. Further re-labelling of tumor
773 cell clusters (labelled as epithelial by SingleR) was performed by InferCNV analysis,
774 demonstrating consistent regions of chromosomal aberration above background rate
775 seen in other cell types²⁶.

776 *Regulatory Network Inference* | For each gene expression cluster, a gene regulatory
777 network was inferred on log-normalized counts by the ARACNe algorithm⁵¹ to identify
778 downstream transcriptional targets of regulatory proteins. ARACNe was run with 100
779 bootstrap iterations using 1785 transcription factors (genes annotated in gene ontology
780 molecular function database as GO:0003700, “transcription factor activity,” or as
781 GO:0003677, “DNA binding” and GO:0030528, “transcription regulator activity,” or as
782 GO:0003677 and GO:0045449, “regulation of transcription”), 668 transcriptional
783 cofactors (a manually curated list, not overlapping with the transcription factor list, built
784 upon genes annotated as GO:0003712, “transcription cofactor activity,” or GO:0030528
785 or GO:0045449), 3455 signaling pathway related genes (annotated in GO biological
786 process database as GO:0007165, “signal transduction” and in GO cellular component

787 database as GO:0005622, “intracellular” or GO:0005886, “plasma membrane”), and
788 3620 surface markers (annotated as GO:0005886 or as GO:0009986, “cell surface”).
789 ARACNe is only run on these gene sets so as to limit protein activity inference to
790 proteins with biologically meaningful downstream regulatory targets, and we do not
791 apply ARACNe to infer regulatory networks for proteins with no known signaling or
792 transcriptional activity for which protein activity may be difficult to biologically interpret.
793 Parameters were set to zero DPI (Data Processing Inequality) tolerance and MI (Mutual
794 Information) p value threshold of 10^{-8} , computed by permuting the original dataset as a
795 null model.

796 *Protein Activity Inference and Clustering* | Inference of protein activity was performed
797 from scaled integrated gene expression matrix and the set of all ARACNe-inferred gene
798 regulatory networks using the VIPER algorithm^{20,22}. Normalized Enrichment Scores of
799 protein activity were successfully inferred on a per-cell basis for 3,437 regulatory
800 proteins. This protein activity matrix was re-clustered in Seurat using the Louvain
801 algorithm on top50 principal components and clustering resolution parameter optimized
802 by silhouette score, as above, with two-dimensional data projection visualized by
803 UMAP. Differential protein activity between clusters was computed by Wilcoxon rank-
804 sum test with multiple testing correction. Differential abundance of each cluster per
805 patient by treatment group was also assessed by Wilcoxon-rank-sum test, as well as
806 differential abundance of each cluster within the combination-treatment group between
807 patients with and without disease recurrence. Cell clusters inferred by SingleR as
808 lymphoid lineage, myeloid lineage, or tumor cells, respectively, were each isolated for
809 further sub-clustering analyses.

810 *Single-cell RNA-seq T/NK Subclustering* | Subsetting lymphoid cells from initial analysis
811 resulted in a VIPER matrix of 14,208 cells, projected into their first 50 principal
812 components using Seurat's RunPCA function, followed by using Seurat's RunUMAP
813 function with method umap-learn. Unsupervised clustering of lymphoid cells was
814 performed by the same silhouette score optimized Louvain approach as above. In
815 addition to SingleR cell type labelling, we applied GSEA on cell-by-cell basis using an
816 expression-based T-reg marker gene set previously published from Obradovic et. al.
817 Cell 2021²², to identify the T-reg cluster. VIPER activity of manually selected relevant

818 markers was also visualized for lymphoid cell subtype identification of all other clusters.
819 Differential abundance of each cluster as percent of lymphoid cells was assessed by
820 treatment group and by recurrence vs non-recurrence within the combination-treatment
821 group, by Wilcox rank-sum test. The ADT-only treatment group was not stratified due to
822 insufficient recurrences for statistical power and recurrence data were not available in
823 the untreated group. Further testing in the combination treatment group of association
824 between Treg abundance and time-to-recurrence was performed by Kaplan-Meier
825 analysis, with optimal cut-point of high-Treg vs low-Treg samples determined by log-
826 rank maximization, and p-value assessed by Cox regression.

827 *Single-cell RNA-seq Myeloid Cell Subclustering* | Isolation of myeloid cells (clusters
828 identified by SingleR as predominantly Monocyte or Macrophage) yielded 5771 Myeloid
829 cells, subclustered in the same manner as lymphoid cells above. RunPCA and
830 RunUMAP from Seurat were used to compute the first 50 principal components and
831 UMAP respectively. Upon sub-clustering, a subpopulation identified as fibroblasts
832 (n=183) by SingleR with the BlueprintEncode reference dataset from Celldex was
833 removed from downstream analysis. A 7-cluster unsupervised clustering solution was
834 selected as optimal by maximization of silhouette score. Clusters were then annotated
835 by cell type with a combination of visualizing manually selected phenotypic markers and
836 assessing Gene Set Enrichment of differentially active proteins by cluster.

837 *Correlation Between FCGR3A Activity and Treg Frequency* | In order to assess for
838 relationship between FCGR3A protein activity among myeloid cells and Treg frequency,
839 we performed correlative analysis between Treg frequency as a percent of lymphoid
840 cells for each patient against average FCGR3A protein activity for myeloid cells as a
841 whole in the same patient, as well as for the specific subset of TREM2+ TAMs.
842 Stratifying these analyses by treatment group shows treatment-dependent association
843 between FCGR3A activity and Treg abundance, such that in combination-treatment
844 alone higher myeloid FCGR3A activity was found to associate with lower Treg
845 abundance.

846 *Single-cell RNA-seq CD8+ T Cell Subclustering* | Upon sub-clustering lymphoid cells,
847 we further isolated the two identified clusters of CD8 T-cells (CD8-1 and CD8-2) for
848 deeper sub-phenotyping. This yielded a VIPER protein activity matrix for 7,475 cells.

849 Re-clustering on the top50 principal components of this matrix yielded a four-cluster
850 solution such that one small subset of n=187 cells appeared to be naïve CD8s or
851 potential contamination, and were removed. This conclusion was supported by GSEA
852 on the gene expression signatures of these cells with the Naive CD8 gene set from
853 Zheng et al. 2021³⁴. The remaining true CD8+ cells were re-scaled and re-clustered
854 yielding a three-cluster solution. These clusters were labelled as “Central Memory”,
855 “Effector” and “Effector/Resident Memory” by Gene Set Enrichment Analysis. “Memory
856 vs Effector” and “Effector vs Memory” signatures were generated using a Mann-Whitney
857 U-Test between the gene expression profiles of CD8+ Trm and CD8+ cytotoxic
858 populations reported by Tuong et al. 2021³¹. The top genes from each of these
859 signatures and in the signatures from Zheng et al. 2021³⁴ were supplied as gene sets to
860 GSEA to compute enrichment on the gene expression profiles of our CD8+ cells.
861 Relevant manually curated marker genes were further visualized by VIPER activity per
862 cluster. Cluster frequencies by treatment group were then calculated to identify changes
863 in these CD8+ subtypes in response to treatment.

864 **Immunofluorescence**

865 Archival FFPE prostate tumor specimens were selected by a board-certified pathologist.
866 Immunoblock slides and representative adjacent H&E slides were sectioned at 5µm by
867 the Herbert Irving Comprehensive Cancer Center’s Molecular Pathology Shared
868 Research (HICCC MPSR). Tissue sections were deparaffinized using a standard series
869 of xylene and ethanol washes and rinsed with distilled water. Antigen retrieval was
870 performed by heating the slides in citrate buffer at pH of 6.0 for 20 minutes in a pressure
871 cooker. Slides were incubated overnight at 4°C with primary antibodies against CD4
872 (1:200, Abcam) and FOXP3 (1:100, Invitrogen). Subsequently, the slides were
873 incubated for 30 minutes at room temperature with horse anti-mouse antibody (1:200,
874 Vector Laboratories), and then for 30 minutes with Streptavidin, Alexa Fluor™ 594
875 conjugate (1:1000, Invitrogen). Next, the slides were incubated for 30 minutes at room
876 temperature with goat anti-rabbit antibody (1:200, Vector Laboratories) and then for an
877 additional 30 minutes with Streptavidin, Alexa Fluor™ 488 conjugate (1:300, Invitrogen).
878 Slide sections were mounted at room temperature with 25µL of VECTASHIELD

879 Vibrance® Antifade Mounting Medium with DAPI (Vector Laboratories) and
880 coverslipped.
881 Fluorescent images were acquired by the Phenolmager™ HT Instrument (Akoya
882 Biosciences). Onboard spectral unmixing was performed using the Phenolmager HT 2.0
883 software (Akoya Biosciences). The images were analyzed with QuPath version 0.5.1⁵².
884 Regions of interest were generated referencing tumor-marked H&E slides from adjacent
885 sections. Nuclear and cell segmentation were performed using the QuPath extension
886 StarDist 0.4.0 with the pretrained model dsb2018_heavy_augment.pb⁵³. Following
887 cellular segmentation, object classifiers were trained on each image to quantify Tregs
888 (CD4+/FOXP3+) per mm² or as a percentage of all DAPI+ cells.

889 **Mice**

890 Male FVB mice were purchased from Jackson Laboratory (Bar Harbor, ME). Mice were
891 8-10 weeks old at time of use. All animals were housed in strict accordance with NIH
892 and American Association of Laboratory Animal Care regulations. All experiments and
893 procedures for this study were approved by the Mayo Clinic Institutional Animal Care
894 and Use Committee (IACUC).

895 **Animal Studies**

896 Myc-CaP cells were provided as a kind gift from Dr. Charles Drake and were verified as
897 free of pathogen and cell line contamination using a 19-marker mouse STR panel
898 through IDEXX BioAnalytics (Columbia, MO). Myc-CaP cells were passaged in RPMI
899 medium (Corning; Corning, NY) supplemented with 10% FBS (Corning; Corning, NY),
900 100 U/mL penicillin, and 100 mg/mL streptomycin (Gibco; Gaithersburg, MD). For tumor
901 implantation, Myc-CaP cells at 70-90% confluence were harvested with 0.05% trypsin
902 (Corning; Corning, NY), washed with PBS, counted, and resuspended at 10x10⁶
903 cells/mL in ice cold PBS. On day 0, 8–10-week-old mice were implanted on the right
904 flank with 1x10⁶ Myc-CaP cells. Cages were randomized to treatment groups after
905 cages were manually normalized to reduce intergroup variability, using the final tumor
906 volume measurement values available prior to treatment. Tumor measurements were
907 recorded in X, Y, and Z dimensions in a non-blinded fashion (largest diameter, smallest
908 diameter, and largest height, respectively) every 2-3 days by digital caliper and tumor

909 volume was calculated by multiplying $X*Y*Z$. On day 24 when tumors were
910 approximately 200mm^3 on average, mice received a single subcutaneous injection in
911 the neck scruff of 625 ug degarelix acetate (ADT; Cayman Chemical; Ann Arbor, MI)
912 resuspended in 100 μl sterile water per mouse. Appropriate treatment groups
913 additionally received anti-CTLA4 (D) (9D9-mIgG2a) or anti-CTLA4 (ND) (9D9-mIgG2a-
914 LALAPG) as indicated by intraperitoneal (IP) injection at 100 μg per mouse in 100 μl
915 sterile PBS on days 24, 27, and 30. Antibodies were purchased from BioXCell
916 (Lebanon, NH). For flow cytometry analysis, cohorts of animals were euthanized on day
917 32 for tissue collection and processing. For survival analysis, mice were deemed eligible
918 for euthanasia when tumor volume exceeded $1,000\text{mm}^3$ or tumor ulceration exceeded
919 5 mm in diameter.

920 **Spectral Flow Cytometry**

921 *Tissue harvest and dissociation* | Following mouse euthanasia, tumor-draining inguinal
922 lymph nodes were dissected and placed in 48-well plates containing 150 μl R10 media
923 on ice. Tumors were harvested, massed, and up to 50 mg tumor was diced and placed
924 in X-Vivo 15 media (Lonza; Basel, Switzerland) in 15mL Eppendorf tubes on ice. DNase
925 (40 μl of 20 mg/mL solution; Roche; Basel, Switzerland) and Collagenase D (125 μl of
926 40 mg/mL solution; Roche; Basel, Switzerland) were added to tumor samples prior to
927 incubation on a shaker at 37°C for 30 minutes. Digest reactions were quenched by
928 adding 5mL R10 media. Tumor digests were filtered through 70 μm filters (Miltenyi;
929 Bergisch Gladbach, GE), remaining undigested tissue was mashed with the handle end
930 of a 3mL syringe plunger, then filters were washed with 5mL R10 prior to centrifugation.
931 Lymph nodes were physically disaggregated with a 1mL syringe plunger in the 48-well
932 plate. All samples were then transferred in R10 into U-bottom 96-well plates for staining.

933 *Staining protocol* | Samples were washed with PBS. Dead cells were stained by
934 resuspension in 100 μl PBS + Live/Dead Fixable Blue dye (1:500; Invitrogen; Waltham,
935 MA). This and all further staining or fixation steps were performed for 30 minutes at
936 room temperature on a plate shaker protected from light, unless specified otherwise.
937 Samples were washed 2x with PBS, then were resuspended in FACS (PBS + 3% FBS
938 + 1mM EDTA + 10mM HEPES) supplemented with TruStain FcX (1:50; BioLegend; San

939 Diego, CA) and TruStain Monocyte Blocker (1:20; BioLegend; San Diego, CA) and
940 placed on ice. Surface antibodies were prepared at optimal dilutions (see
941 Supplementary Table S1) in FACS supplemented with Brilliant Stain Plus buffer (BD;
942 Franklin Lakes, NJ), then were added to samples in blocking solution. After staining,
943 samples were washed 2x with FACS buffer and fixed in 100 μ l of FoxP3
944 Fixation/Permeabilization Kit buffer (eBioscience; San Diego, CA). Samples were
945 washed twice with 1X Permeabilization buffer (1X PW) then were stained in 1X PW plus
946 intracellular antibodies. Plate(s) were sealed and intracellular staining was performed
947 overnight at 4^o C on an orbital shaker. Samples were then washed twice in FACS then
948 resuspended in 200 μ l FACS and were immediately acquired on a Cytex Aurora 5-laser
949 (UV/V/B/YG/R) cytometer. Simultaneously stained splenocyte samples or SpectraComp
950 beads (Slingshot Biosciences; Emeryville, CA) were utilized for single stain controls as
951 indicated in Supplemental Table S1.

952 **Analysis of Mass Cytometry and Flow Cytometry Data**

953 All analysis was performed using FlowJo (BD; San Diego, CA). Live, single cell, CD45+
954 events from all files were identified by manual gating using conventional gating
955 strategies for CyTOF and flow cytometry data as shown in Extended Data Fig 5-6.
956 Samples with fewer than 1,000 live CD45+ single cell events were excluded from further
957 analysis. All live CD45+ single cell events in the CyTOF data were concatenated for
958 high dimensional analyses, while up to 50,000 live CD45+ single cell events from the
959 flow cytometry dataset were downsampled and concatenated for downstream analysis.
960 Canonical immune lineages in both datasets were defined in a semi-supervised manner
961 utilizing FlowSOM²⁷. Data were purposely overclustered to 30 FlowSOM-derived
962 clusters based on expression of lineage-defining markers in each panel. These clusters
963 were then manually collated based on lineage marker expression to obtain the minimal
964 possible number of canonical immune lineages. Clusters were embedded in two-
965 dimensional space for visualization using the supervised UMAP function in FlowJo,
966 which performs dimensionality reduction based on selected lineage-defining marker
967 expression with incorporation of FlowSOM-derived clusters as a weighted parameter.
968 For discovery-based subclustering of individual lineages (e.g. CD4 Tregs), an additional
969 round of semi-supervised FlowSOM was performed in an analogous manner as

970 described above; involving FlowSOM-derived overclustering based on phenotypic
971 markers differentially expressed by cells within the lineage of interest, followed by
972 manual collation of clusters into minimal number of phenotypically distinct subclusters.
973 For visualization of discovery-based subclustering within lineages, we utilized
974 PaCMAP⁵⁴ dimensionality reduction to embed data in two dimensions. Absolute cell
975 numbers and mean geometric fluorescent intensity (gMFI) data was exported for each
976 cluster for downstream analysis. Phenotypic marker data was scaled based on the
977 minimum and maximum gMFI values of each given marker across all live CD45+ cells
978 or within the lineage of interest, as indicated in the figure legends.

979 **Statistical Analyses**

980 Baseline patient characteristics and study outcomes were computed and visualized
981 utilizing the gtsummary package (v 1.7.2)⁵⁵, in Rstudio (R version 4.3.1, 2023-06-16).
982 Mutational profiles were visualized using Oviz-Bio's LandScape (v1.1.1)⁵⁶. Stratification
983 for Kaplan Meier analyses was performed using log-rank maximization algorithm as
984 implemented in the survminer package. CyTOF and spectral flow cytometry statistical
985 testing was conducted in GraphPad Prism (v10.2). All other quantitative and statistical
986 analyses were performed using the R computational environment and packages
987 described above. Differential gene expression was assessed at the single-cell level by
988 the MAST single-cell statistical framework as implemented in Seurat v4⁵⁷, and
989 differential VIPER activity was assessed by Wilcoxon rank-sum test, each with
990 Benjamini-Hochberg multiple-testing correction. Unless otherwise noted, comparisons
991 of cell frequencies by treatment group were performed by Student's t-test or non-
992 parametric Wilcoxon rank-sum test, and survival analyses were performed by log-rank
993 test. In all cases, statistical significance was defined as an adjusted p value less than
994 0.05. Details of all statistical tests used can be found in the corresponding figure
995 legends.

996
997

998 **Acknowledgments**

999

1000 We would like to acknowledge the Columbia University Human Immune Monitoring
1001 Core (HIMC) for assistance with single cell RNA sequencing and the Mayo Clinic
1002 Immune Monitoring Core for assistance with CyTOF data acquisition. We would also
1003 like to acknowledge our collaborators at Bristol Myers Squibb for their help in
1004 conducting the study. Most of all we thank the patients and their families for participating
1005 in this study.
1006

1007 **Extended Data**

1008

1009 **Extended Data Figure 1: NeoRED-P study co-mutation plot. (A)** Co-mutation plot of

1010 NeoRED-P patients and stage matched untreated control cohort.

1011

1012 **Extended Data Figure 2: PSA responses and testosterone recovery of all trial**

1013 **participants. (A)** Median serum PSA (dark blue line; round dots) and testosterone (light

1014 blue line; squares) concentrations over time of all patients treated with ADT only. Error

1015 bars denote interquartile range. **(B)** Median serum PSA (dark red line; round dots) and

1016 testosterone (light red line; squares) concentrations of all patients treated with ADT +

1017 anti-CTLA4-NF. Error bars denote interquartile range. **(C)** Plots of serum PSA and

1018 testosterone concentrations for individual patients treated with ADT only. **(D)** Plots of

1019 serum PSA and testosterone concentrations for individual patients treated with ADT +

1020 anti-CTLA4-NF. D = day; P or RP = radical prostatectomy; M or Mo = month.

1021

1022 **Extended Data Figure 3: Single cell RNA sequencing QC and inferCNV results. (A)**

1023 Violin plots representing quality control plots of scRNAseq data stratified by treatment

1024 group, including number of unique molecular identifiers (UMIs) per cell (left), number of

1025 unique genes detected per cell (middle), and percent mitochondrial gene content per

1026 cell (right). **(B)** Plots representing outcomes of InferCNV analysis through visualization

1027 of inferred copy number aberrations. Reference immune and stromal cell populations

1028 shown above, and clusters annotated as tumor cells shown at bottom.

1029

1030 **Extended Data Figure 4: Comparison of single cell RNA sequencing and CyTOF**
1031 **datasets. (A)** Representative gating strategy representing isolation of viable, single cell
1032 CD45+ cells in the CyTOF dataset. **(B)** Pearson correlation plots comparing frequency
1033 of immune lineages annotated during clustering of both CyTOF and scRNAseq datasets
1034 as a percent of total cells. **(C)** Violin plots representing frequency and distribution of all
1035 lineage frequencies as percent of total cells by scRNAseq, stratified by treatment group.
1036 **(D)** Violin plots representing frequency and distribution of all lineage frequencies as
1037 percent of total cells by CyTOF, stratified by treatment group. **(E)** Violin plot
1038 representing frequency of T/NK subclusters as a percent of all cells, stratified by post-
1039 surgical 2-year recurrence status. Student's t-test was used to evaluate statistical
1040 significance. **(F)** Kaplan-Meier curve representing time-to-PSA recurrence in ADT-
1041 treated patients stratified by Treg frequency in scRNAseq data. Log-rank test was
1042 performed to evaluate statistical significance.

1043

1044 **Extended Data Figure 5: Additional flow cytometry data related to DC modulation**
1045 **by ADT + anti-CTLA4 (D) in the MycCaP model. (A)** Representative gating strategy of
1046 viable, single cell CD45+ cells in the spectral flow cytometry dataset derived from **(A)**
1047 tumor and **(B)** tumor draining lymph nodes. Summary of downstream analytical
1048 workflow shown at right. **(C)** Heatmap of relevant phenotypic marker expression across
1049 all tumor-infiltrating DC clusters. Data represents median MFI for each marker
1050 normalized to the minimum and maximum values across all DC clusters. Any markers
1051 exhibiting uniform low expression were normalized to the minimum and maximum
1052 values across all immune clusters to demonstrate low expression levels across clusters.

1053 **(D)** Violin plots representing relative proportions of DC clusters as a percentage of all
1054 DCs in the indicated treatment groups. Two-way ANOVA with Tukey multiple testing
1055 correction was used to assess statistical significance. **(E)** Violin plots representing the
1056 frequency of PD-L2+ DCs as a percentage of DCs (left) or as a percentage of CD45
1057 (right) in a second independent replicate experiment. Student's t-test was used to
1058 assess statistical significance.

1059

1060 **Extended Data Figure 6: Additional CD8 phenotyping data by scRNAseq, CyTOF,**

1061 **and flow cytometry. (A)** UMAP plot representing subclustering of combined CD8-1 and

1062 CD8-2 clusters in the original T/NK cluster, identifying 4 phenotypically unique

1063 subclusters. **(B)** Violin plots representing expression of *Cd8a* and *Cd4*, VIPER inferred

1064 protein activity of *CCR7*, and tumor-infiltrating naïve CD8 T cell GSEA scores (derived

1065 from Zheng *et al.* 2021) on a per cell basis in the scRNAseq dataset, stratified by

1066 subcluster. **(C)** Heatmap of relevant phenotypic marker expression across all tumor-

1067 infiltrating CD8 clusters in the CyTOF. Data represents geometric MFI for each marker

1068 normalized to the minimum and maximum values across all CD8 clusters. Any markers

1069 exhibiting uniform high or low expression were normalized to the minimum and

1070 maximum values across all immune clusters to demonstrate high or low expression

1071 levels across clusters, respectively. **(D)** Violin plots representing relative proportions of

1072 CD8 clusters as a percentage of all CD8s in the indicated treatment groups. Two-way

1073 ANOVA with Tukey multiple testing correction was used to assess statistical

1074 significance. **(E)** Heatmap of relevant phenotypic marker expression across all tumor-

1075 infiltrating CD4 Tconv clusters in the CyTOF. Data represents geometric MFI for each

1076 marker normalized to the minimum and maximum values across all CD4 Tconv clusters.
1077 Any markers exhibiting uniform high or low expression were normalized to the minimum
1078 and maximum values across all immune clusters to demonstrate high or low expression
1079 levels across clusters, respectively. **(F)** Violin plots representing relative proportions of
1080 CD4 Tconv clusters as a percentage of all CD4 Tconv cells in the indicated treatment
1081 groups. Two-way ANOVA with Tukey multiple testing correction was used to assess
1082 statistical significance. **(G)** Heatmap of relevant phenotypic marker expression across
1083 all tumor-infiltrating CD8 clusters in the mouse spectral flow cytometry data. Data
1084 represents median MFI for each marker normalized to the minimum and maximum
1085 values across all CD8 clusters. Any markers exhibiting uniform high or low expression
1086 were normalized to the minimum and maximum values across all immune clusters to
1087 demonstrate high or low expression levels across clusters, respectively. **(D)** Violin plots
1088 representing relative proportions of CD8 clusters as a percentage of all CD8s in the
1089 indicated treatment groups. Two-way ANOVA with Tukey multiple testing correction was
1090 used to assess statistical significance. **(I)** Violin plots representing the frequency of
1091 CD39+41BB+ CD8s as a percentage of tumor-infiltrating CD8s (left) or as a percentage
1092 of CD45 (right) in a second independent replicate experiment. Student's t-test was used
1093 to assess statistical significance. **(J)** Violin plots representing the frequency of
1094 CD44⁺Ki67⁺ CD8s as a percentage of tdLN CD8s (left) or CD44⁺Ki67⁺ CD4 Tconv cells
1095 as a percentage of tdLN CD4 Tconv cells (right) in a second independent replicate
1096 experiment. Student's t-test was used to assess statistical significance. **(K)** Violin plots
1097 representing the frequency of Tregs as a percentage of all tdLN CD45⁺ cells stratified by
1098 treatment group. Student's t-test was used to assess statistical significance.

References

- 1 Venturini, N. J. & Drake, C. G. Immunotherapy for Prostate Cancer. *Cold Spring Harb Perspect Med* **9** (2019). <https://doi.org/10.1101/cshperspect.a030627>
- 2 Le, D. T. *et al.* Phase II Open-Label Study of Pembrolizumab in Treatment-Refractory, Microsatellite Instability-High/Mismatch Repair-Deficient Metastatic Colorectal Cancer: KEYNOTE-164. *J Clin Oncol* **38**, 11-19 (2020). <https://doi.org/10.1200/jco.19.02107>
- 3 Gratzke, C. *et al.* KEYNOTE-991: pembrolizumab plus enzalutamide and androgen deprivation for metastatic hormone-sensitive prostate cancer. *Future Oncol* (2023). <https://doi.org/10.2217/fon-2022-0776>
- 4 Powles, T. *et al.* Atezolizumab with enzalutamide versus enzalutamide alone in metastatic castration-resistant prostate cancer: a randomized phase 3 trial. *Nat Med* **28**, 144-153 (2022). <https://doi.org/10.1038/s41591-021-01600-6>
- 5 Petrylak, D. P. *et al.* KEYNOTE-921: Phase III study of pembrolizumab plus docetaxel for metastatic castration-resistant prostate cancer. *Future Oncol* **17**, 3291-3299 (2021). <https://doi.org/10.2217/fon-2020-1133>
- 6 Antonarakis, E. S. *et al.* Pembrolizumab Plus Olaparib for Patients With Previously Treated and Biomarker-Unselected Metastatic Castration-Resistant Prostate Cancer: The Randomized, Open-Label, Phase III KEYLYNK-010 Trial. *J Clin Oncol* **41**, 3839-3850 (2023). <https://doi.org/10.1200/jco.23.00233>
- 7 Beer, T. M. *et al.* Randomized, Double-Blind, Phase III Trial of Ipilimumab Versus Placebo in Asymptomatic or Minimally Symptomatic Patients With Metastatic Chemotherapy-Naive Castration-Resistant Prostate Cancer. *J Clin Oncol* **35**, 40-47 (2017). <https://doi.org/10.1200/jco.2016.69.1584>
- 8 Fizazi, K. *et al.* Final Analysis of the Ipilimumab Versus Placebo Following Radiotherapy Phase III Trial in Postdocetaxel Metastatic Castration-resistant Prostate Cancer Identifies an Excess of Long-term Survivors. *Eur Urol* **78**, 822-830 (2020). <https://doi.org/10.1016/j.eururo.2020.07.032>
- 9 Sharma, P. *et al.* Nivolumab Plus Ipilimumab for Metastatic Castration-Resistant Prostate Cancer: Preliminary Analysis of Patients in the CheckMate 650 Trial. *Cancer Cell* **38**, 489-499.e483 (2020). <https://doi.org/10.1016/j.ccell.2020.08.007>
- 10 Shen, Y. C. *et al.* Combining intratumoral Treg depletion with androgen deprivation therapy (ADT): preclinical activity in the Myc-CaP model. *Prostate Cancer Prostatic Dis* **21**, 113-125 (2018). <https://doi.org/10.1038/s41391-017-0013-x>
- 11 Obradovic, A. Z. *et al.* T-Cell Infiltration and Adaptive Treg Resistance in Response to Androgen Deprivation With or Without Vaccination in Localized Prostate Cancer. *Clin Cancer Res* **26**, 3182-3192 (2020). <https://doi.org/10.1158/1078-0432.Ccr-19-3372>
- 12 Chand, D. *et al.* Botensilimab, an Fc-enhanced anti-CTLA-4 antibody, is effective against tumors poorly responsive to conventional immunotherapy. *Cancer Discov* (2024). <https://doi.org/10.1158/2159-8290.Cd-24-0190>
- 13 Maeda, Y. *et al.* Depletion of central memory CD8(+) T cells might impede the antitumor therapeutic effect of Mogamulizumab. *Nat Commun* **12**, 7280 (2021). <https://doi.org/10.1038/s41467-021-27574-0>

- 14 Rudin, C. M. *et al.* SKYSCRAPER-02: Tiragolumab in Combination With Atezolizumab Plus Chemotherapy in Untreated Extensive-Stage Small-Cell Lung Cancer. *J Clin Oncol* **42**, 324-335 (2024). <https://doi.org/10.1200/jco.23.01363>
- 15 Luke, J. J., Zha, Y., Matijevich, K. & Gajewski, T. F. Single dose denileukin diftitox does not enhance vaccine-induced T cell responses or effectively deplete Tregs in advanced melanoma: immune monitoring and clinical results of a randomized phase II trial. *J Immunother Cancer* **4**, 35 (2016). <https://doi.org/10.1186/s40425-016-0140-2>
- 16 Sharma, A. *et al.* Anti-CTLA-4 Immunotherapy Does Not Deplete FOXP3(+) Regulatory T Cells (Tregs) in Human Cancers. *Clinical cancer research : an official journal of the American Association for Cancer Research* **25**, 1233-1238 (2019). <https://doi.org/10.1158/1078-0432.CCR-18-0762>
- 17 Arce Vargas, F. *et al.* Fc Effector Function Contributes to the Activity of Human Anti-CTLA-4 Antibodies. *Cancer Cell* **33**, 649-663.e644 (2018). <https://doi.org/10.1016/j.ccell.2018.02.010>
- 18 VanDerMeid, K. R. *et al.* Cellular Cytotoxicity of Next-Generation CD20 Monoclonal Antibodies. *Cancer Immunol Res* **6**, 1150-1160 (2018). <https://doi.org/10.1158/2326-6066.Cir-18-0319>
- 19 Nava Rodrigues, D. *et al.* Immunogenomic analyses associate immunological alterations with mismatch repair defects in prostate cancer. *J Clin Invest* **128**, 4441-4453 (2018). <https://doi.org/10.1172/jci121924>
- 20 Alvarez, M. J. *et al.* Functional characterization of somatic mutations in cancer using network-based inference of protein activity. *Nature genetics* **48**, 838-847 (2016). <https://doi.org/10.1038/ng.3593>
- 21 Vlahos, L. *et al.* Systematic, Protein Activity-based Characterization of Single Cell State. *bioRxiv*, 2021.2005.2020.445002 (2023). <https://doi.org/10.1101/2021.05.20.445002>
- 22 Obradovic, A. *et al.* Single-cell protein activity analysis identifies recurrence-associated renal tumor macrophages. *Cell* **184**, 2988-3005.e2916 (2021). <https://doi.org/10.1016/j.cell.2021.04.038>
- 23 Obradovic, A. *et al.* Systematic elucidation and pharmacological targeting of tumor-infiltrating regulatory T cell master regulators. *Cancer Cell* **41**, 933-949.e911 (2023). <https://doi.org/10.1016/j.ccell.2023.04.003>
- 24 Aran, D. *et al.* Reference-based analysis of lung single-cell sequencing reveals a transitional profibrotic macrophage. *Nat Immunol* **20**, 163-172 (2019). <https://doi.org/10.1038/s41590-018-0276-y>
- 25 Patel, A. P. *et al.* Single-cell RNA-seq highlights intratumoral heterogeneity in primary glioblastoma. *Science* **344**, 1396-1401 (2014). <https://doi.org/10.1126/science.1254257>
- 26 De Falco, A., Caruso, F., Su, X.-D., Iavarone, A. & Ceccarelli, M. A variational algorithm to detect the clonal copy number substructure of tumors from scRNA-seq data. *Nat Commun* **14**, 1074 (2023). <https://doi.org/10.1038/s41467-023-36790-9>
- 27 Van Gassen, S. *et al.* FlowSOM: Using self-organizing maps for visualization and interpretation of cytometry data. *Cytometry A* **87**, 636-645 (2015). <https://doi.org/10.1002/cyto.a.22625>

- 28 Zhao, S. G. *et al.* The Immune Landscape of Prostate Cancer and Nomination of PD-L2 as a Potential Therapeutic Target. *JNCI: Journal of the National Cancer Institute* **111**, 301-310 (2018). <https://doi.org/10.1093/jnci/djy141>
- 29 Simpson, T. R. *et al.* Fc-dependent depletion of tumor-infiltrating regulatory T cells co-defines the efficacy of anti-CTLA-4 therapy against melanoma. *J Exp Med* **210**, 1695-1710 (2013). <https://doi.org/10.1084/jem.20130579>
- 30 Selby, M. J. *et al.* Anti-CTLA-4 Antibodies of IgG2a Isotype Enhance Antitumor Activity through Reduction of Intratumoral Regulatory T Cells. *Cancer Immunology Research* **1**, 32-42 (2013). <https://doi.org/10.1158/2326-6066.cir-13-0013>
- 31 Tuong, Z. K. *et al.* Resolving the immune landscape of human prostate at a single-cell level in health and cancer. *Cell Rep* **37**, 110132 (2021). <https://doi.org/10.1016/j.celrep.2021.110132>
- 32 Schlothauer, T. *et al.* Novel human IgG1 and IgG4 Fc-engineered antibodies with completely abolished immune effector functions. *Protein Eng Des Sel* **29**, 457-466 (2016). <https://doi.org/10.1093/protein/gzw040>
- 33 Maier, B. *et al.* A conserved dendritic-cell regulatory program limits antitumour immunity. *Nature* **580**, 257-262 (2020). <https://doi.org/10.1038/s41586-020-2134-y>
- 34 Zheng, L. *et al.* Pan-cancer single-cell landscape of tumor-infiltrating T cells. *Science* **374**, abe6474 (2021). <https://doi.org/10.1126/science.abe6474>
- 35 Duhén, T. *et al.* Co-expression of CD39 and CD103 identifies tumor-reactive CD8 T cells in human solid tumors. *Nat Commun* **9**, 2724 (2018). <https://doi.org/10.1038/s41467-018-05072-0>
- 36 Bartkowiak, T. & Curran, M. A. 4-1BB Agonists: Multi-Potent Potentiators of Tumor Immunity. *Front Oncol* **5**, 117 (2015). <https://doi.org/10.3389/fonc.2015.00117>
- 37 Marangoni, F. *et al.* Expansion of tumor-associated Treg cells upon disruption of a CTLA-4-dependent feedback loop. *Cell* **184**, 3998-4015.e3919 (2021). [https://doi.org:https://doi.org/10.1016/j.cell.2021.05.027](https://doi.org/https://doi.org/10.1016/j.cell.2021.05.027)
- 38 Knorr, D. A. *et al.* FcγRIIB Is an Immune Checkpoint Limiting the Activity of Treg-Targeting Antibodies in the Tumor Microenvironment. *Cancer Immunology Research* **12**, 322-333 (2024). <https://doi.org/10.1158/2326-6066.Cir-23-0389>
- 39 Ray, A. *et al.* Critical role of CD206+ macrophages in promoting a cDC1-NK-CD8 T cell anti-tumor immune axis. *bioRxiv*, 2023.2010.2031.560822 (2024). <https://doi.org/10.1101/2023.10.31.560822>
- 40 Yofe, I. *et al.* Anti-CTLA-4 antibodies drive myeloid activation and reprogram the tumor microenvironment through FcγR engagement and type I interferon signaling. *Nat Cancer* **3**, 1336-1350 (2022). <https://doi.org/10.1038/s43018-022-00447-1>
- 41 Tan, C. L. *et al.* PD-1 restraint of regulatory T cell suppressive activity is critical for immune tolerance. *Journal of Experimental Medicine* **218** (2020). <https://doi.org/10.1084/jem.20182232>
- 42 Van Damme, H. *et al.* Therapeutic depletion of CCR8(+) tumor-infiltrating regulatory T cells elicits antitumor immunity and synergizes with anti-PD-1

- therapy. *Journal for immunotherapy of cancer* **9**, e001749 (2021).
<https://doi.org/10.1136/jitc-2020-001749>
- 43 Whiteside, S. K. *et al.* CCR8 marks highly suppressive Treg cells within tumours but is dispensable for their accumulation and suppressive function. *Immunology* **163**, 512-520 (2021). <https://doi.org/10.1111/imm.13337>
- 44 Whiteside, S. K. *et al.* Acquisition of suppressive function by conventional T cells limits antitumor immunity upon T_{reg} depletion. *Science Immunology* **8**, eabo5558 (2023). <https://doi.org/doi:10.1126/sciimmunol.abo5558>
- 45 Waight, J. D. *et al.* Selective FcγR Co-engagement on APCs Modulates the Activity of Therapeutic Antibodies Targeting T Cell Antigens. *Cancer Cell* **33**, 1033-1047.e1035 (2018). <https://doi.org/10.1016/j.ccell.2018.05.005>
- 46 Espinosa-Carrasco, G. *et al.* Intratumoral immune triads are required for immunotherapy-mediated elimination of solid tumors. *Cancer Cell* **42**, 1202-1216.e1208 (2024). <https://doi.org/10.1016/j.ccell.2024.05.025>
- 47 Magen, A. *et al.* Intratumoral dendritic cell-CD4(+) T helper cell niches enable CD8(+) T cell differentiation following PD-1 blockade in hepatocellular carcinoma. *Nat Med* **29**, 1389-1399 (2023). <https://doi.org/10.1038/s41591-023-02345-0>
- 48 Kemp Bohan, P. M. *et al.* Correlation of tumor microenvironment from biopsy and resection specimens in untreated colorectal cancer patients: a surprising lack of agreement. *Cancer Immunol Immunother* **70**, 1465-1474 (2021).
<https://doi.org/10.1007/s00262-020-02784-5>
- 49 Gao, J. *et al.* VISTA is an inhibitory immune checkpoint that is increased after ipilimumab therapy in patients with prostate cancer. *Nat Med* **23**, 551-555 (2017).
<https://doi.org/10.1038/nm.4308>
- 50 Sireci, A. N. *et al.* Clinical Genomic Profiling of a Diverse Array of Oncology Specimens at a Large Academic Cancer Center: Identification of Targetable Variants and Experience with Reimbursement. *J Mol Diagn* **19**, 277-287 (2017).
<https://doi.org/10.1016/j.jmoldx.2016.10.008>
- 51 Margolin, A. A. *et al.* ARACNE: An Algorithm for the Reconstruction of Gene Regulatory Networks in a Mammalian Cellular Context. *BMC Bioinformatics* **7**, S7 (2006). <https://doi.org/10.1186/1471-2105-7-S1-S7>
- 52 Bankhead, P. *et al.* QuPath: Open source software for digital pathology image analysis. *Sci Rep* **7**, 16878 (2017). <https://doi.org/10.1038/s41598-017-17204-5>
- 53 Schmidt, U., Weigert, M., Broaddus, C. & Myers, G. 265-273 (Springer International Publishing).
- 54 Huang, H., Wang, Y., Rudin, C. & Browne, E. P. Towards a comprehensive evaluation of dimension reduction methods for transcriptomic data visualization. *Communications Biology* **5**, 719 (2022). <https://doi.org/10.1038/s42003-022-03628-x>
- 55 Sjoberg, D. D., Whiting, K. A., Curry, M., Lavery, J. A. & Larmarange, J. Reproducible Summary Tables with the gtsummary Package. *R J.* **13**, 570 (2021).
- 56 Jia, W., Li, H., Li, S., Chen, L. & Li, S. C. Oviz-Bio: a web-based platform for interactive cancer genomics data visualization. *Nucleic Acids Res* **48**, W415-w426 (2020). <https://doi.org/10.1093/nar/gkaa371>

- 57 Finak, G. *et al.* MAST: a flexible statistical framework for assessing transcriptional changes and characterizing heterogeneity in single-cell RNA sequencing data. *Genome Biology* **16**, 278 (2015).
<https://doi.org/10.1186/s13059-015-0844-5>

Figure 1

It is made available under a [CC-BY-NC-ND 4.0 International license](https://creativecommons.org/licenses/by-nc-nd/4.0/).

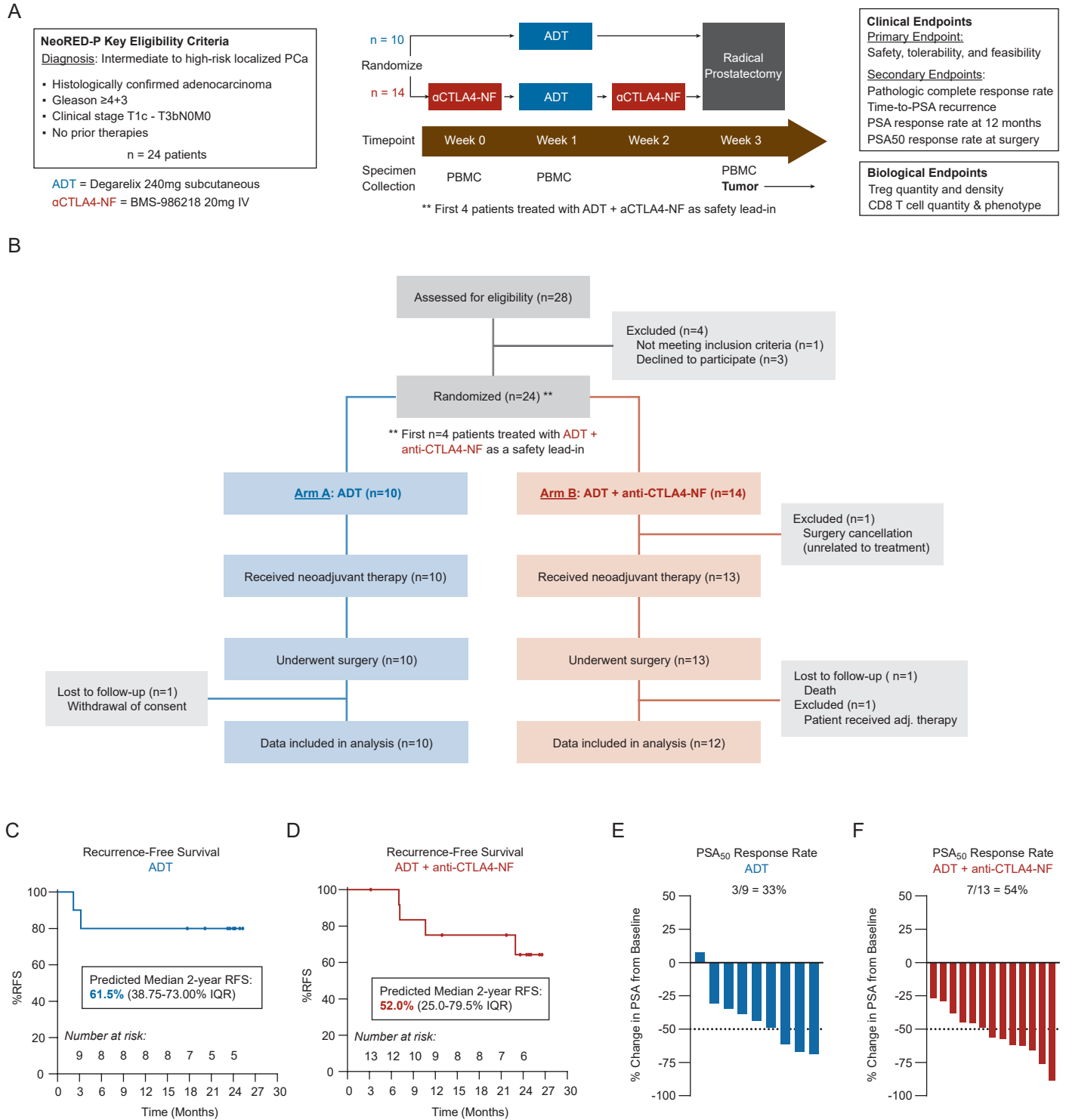


Figure 2

It is made available under a [CC-BY-NC-ND 4.0 International license](https://creativecommons.org/licenses/by-nc-nd/4.0/).

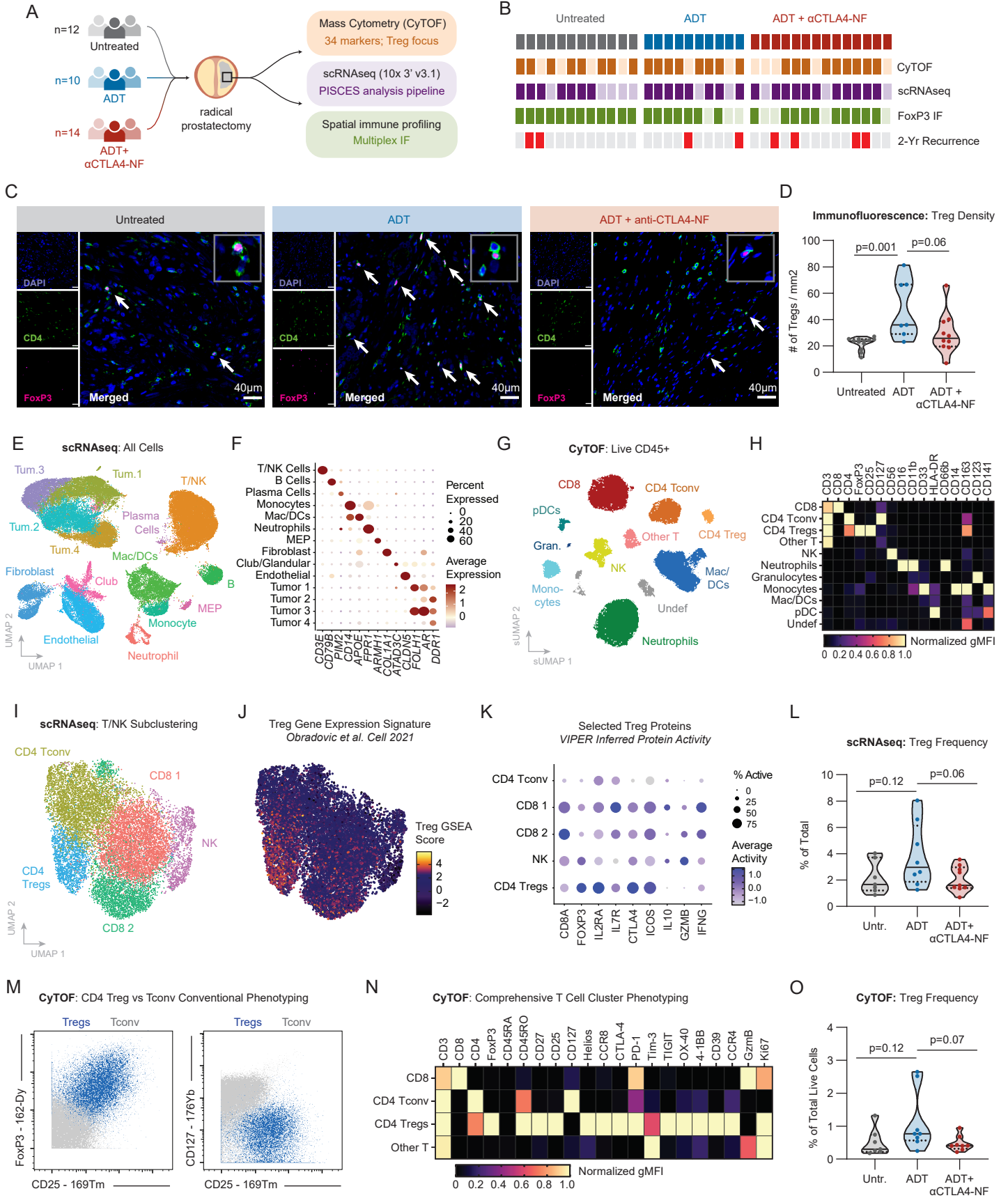


Figure 3

It is made available under a [CC-BY-NC-ND 4.0 International license](https://creativecommons.org/licenses/by-nc-nd/4.0/).

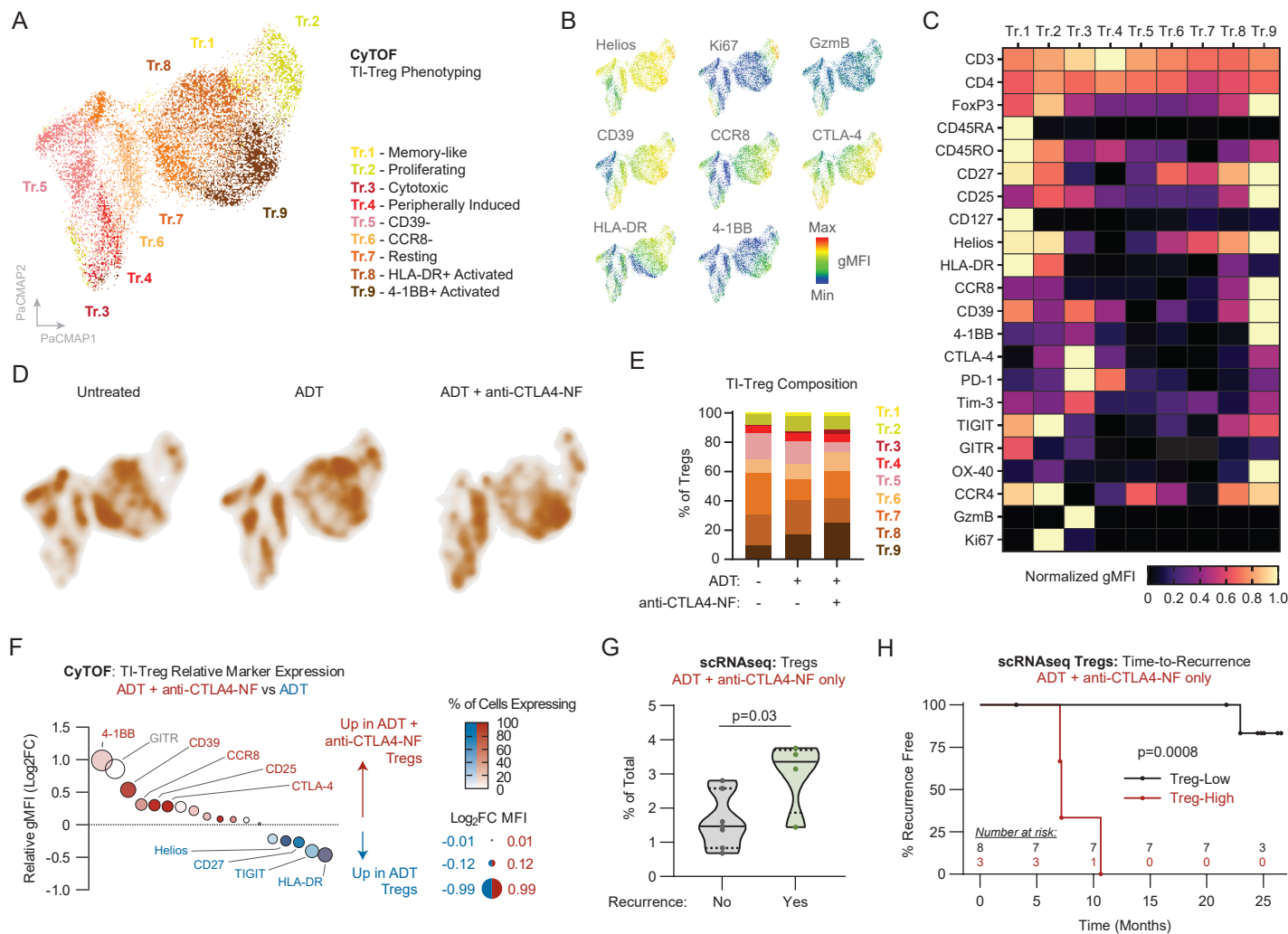


Figure 4

It is made available under a [CC-BY-NC-ND 4.0 International license](https://creativecommons.org/licenses/by-nc-nd/4.0/).

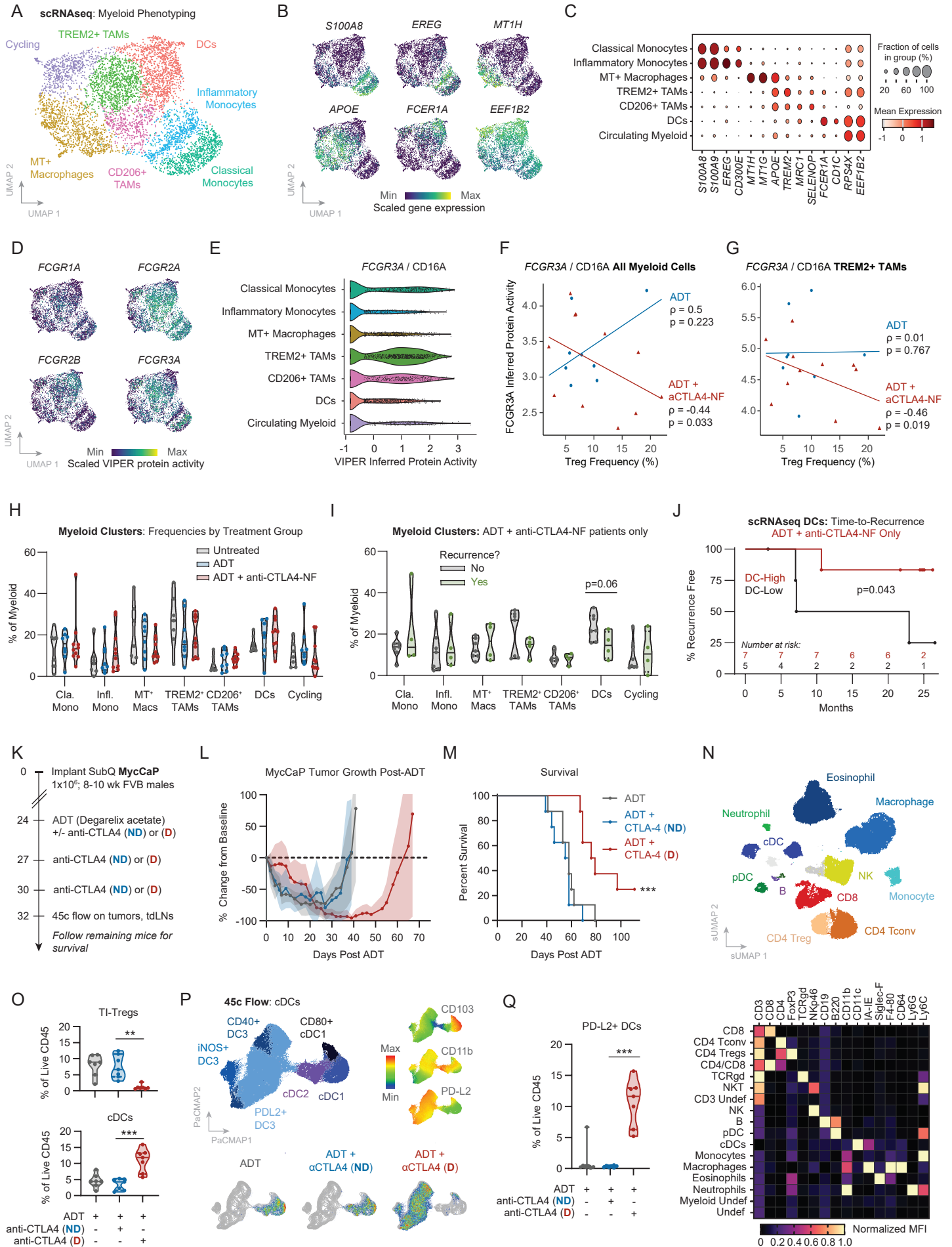
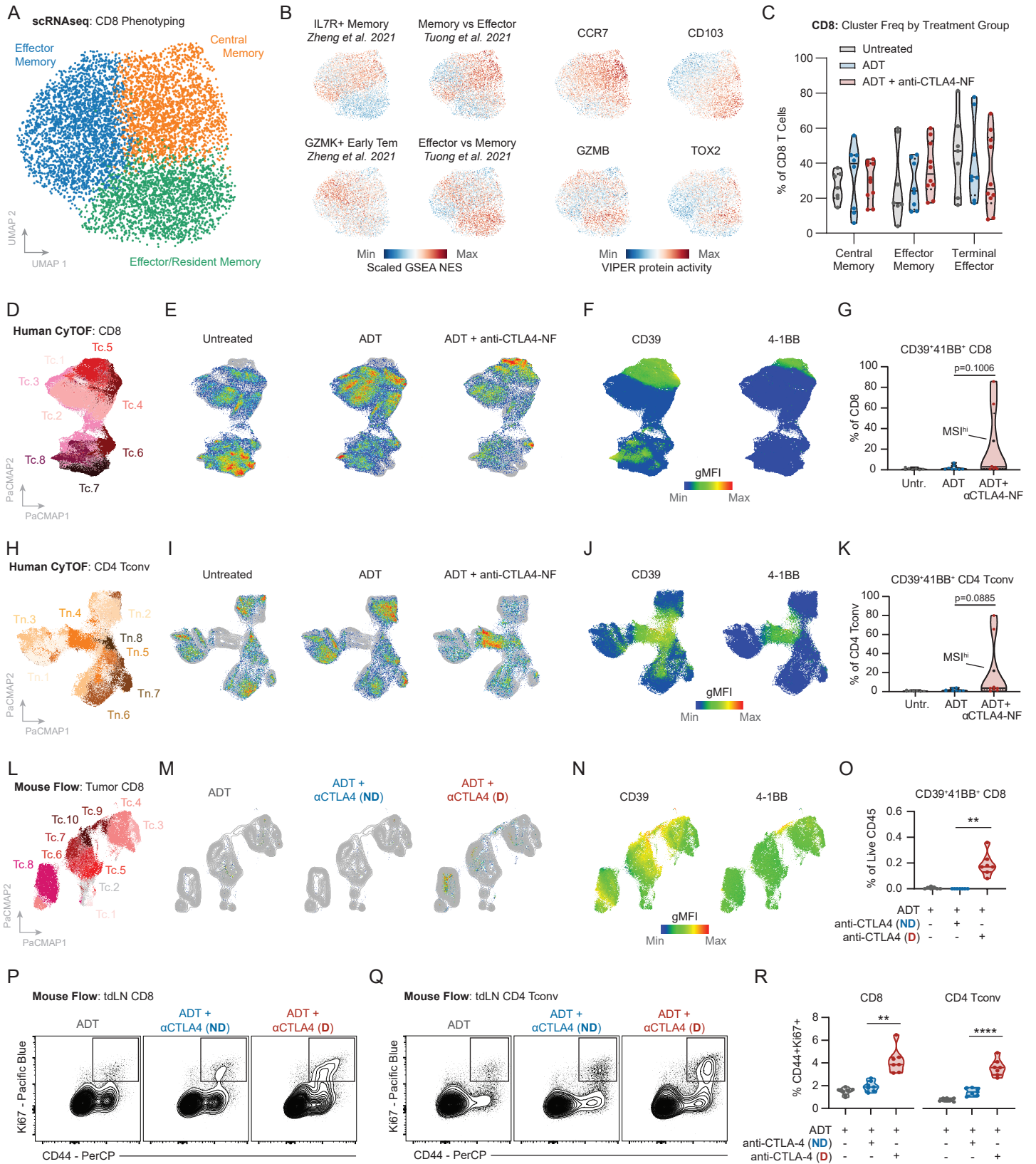


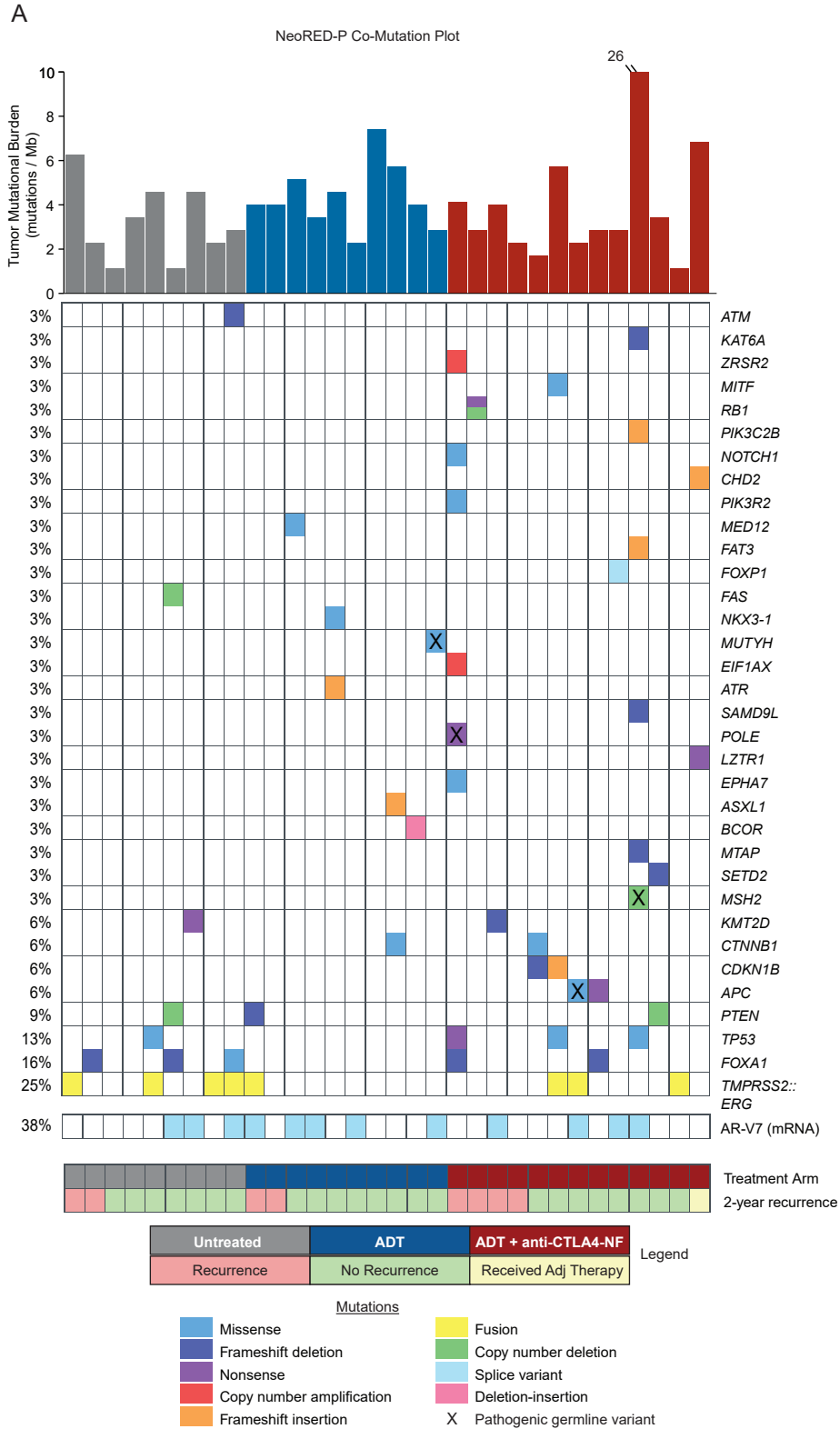
Figure 5

It is made available under a [CC-BY-NC-ND 4.0 International license](https://creativecommons.org/licenses/by-nc-nd/4.0/).



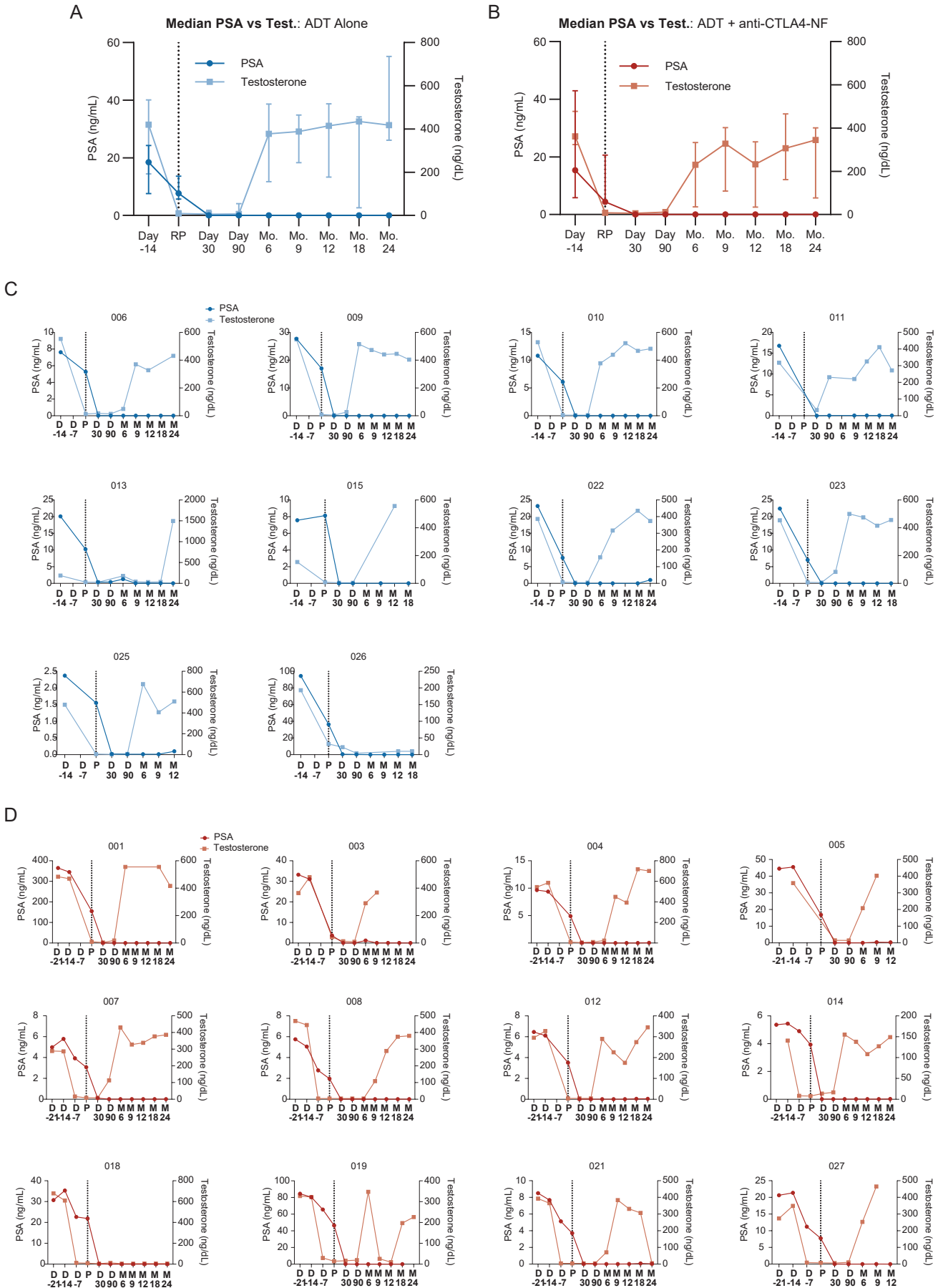
Extended Data Figure 1

It is made available under a [CC-BY-NC-ND 4.0 International license](https://creativecommons.org/licenses/by-nc-nd/4.0/).



Extended Data Figure 2

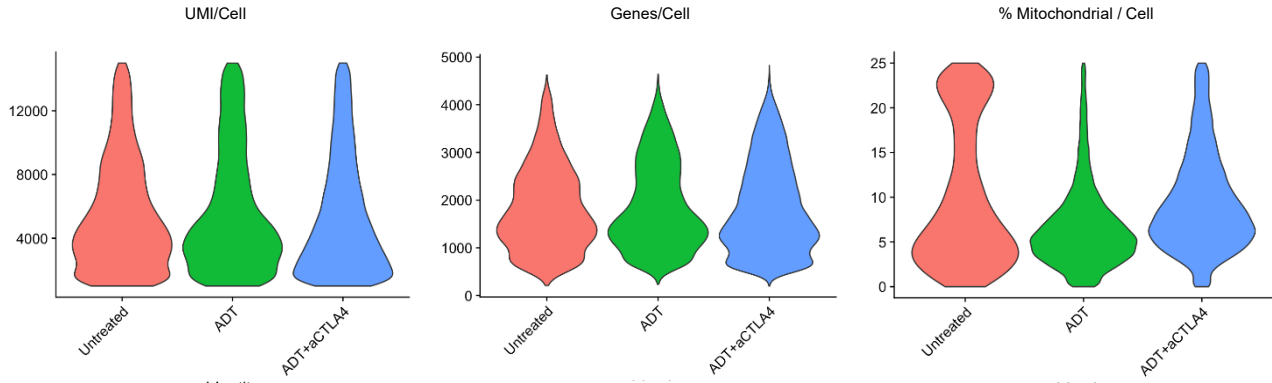
It is made available under a [CC-BY-NC-ND 4.0 International license](https://creativecommons.org/licenses/by-nc-nd/4.0/).



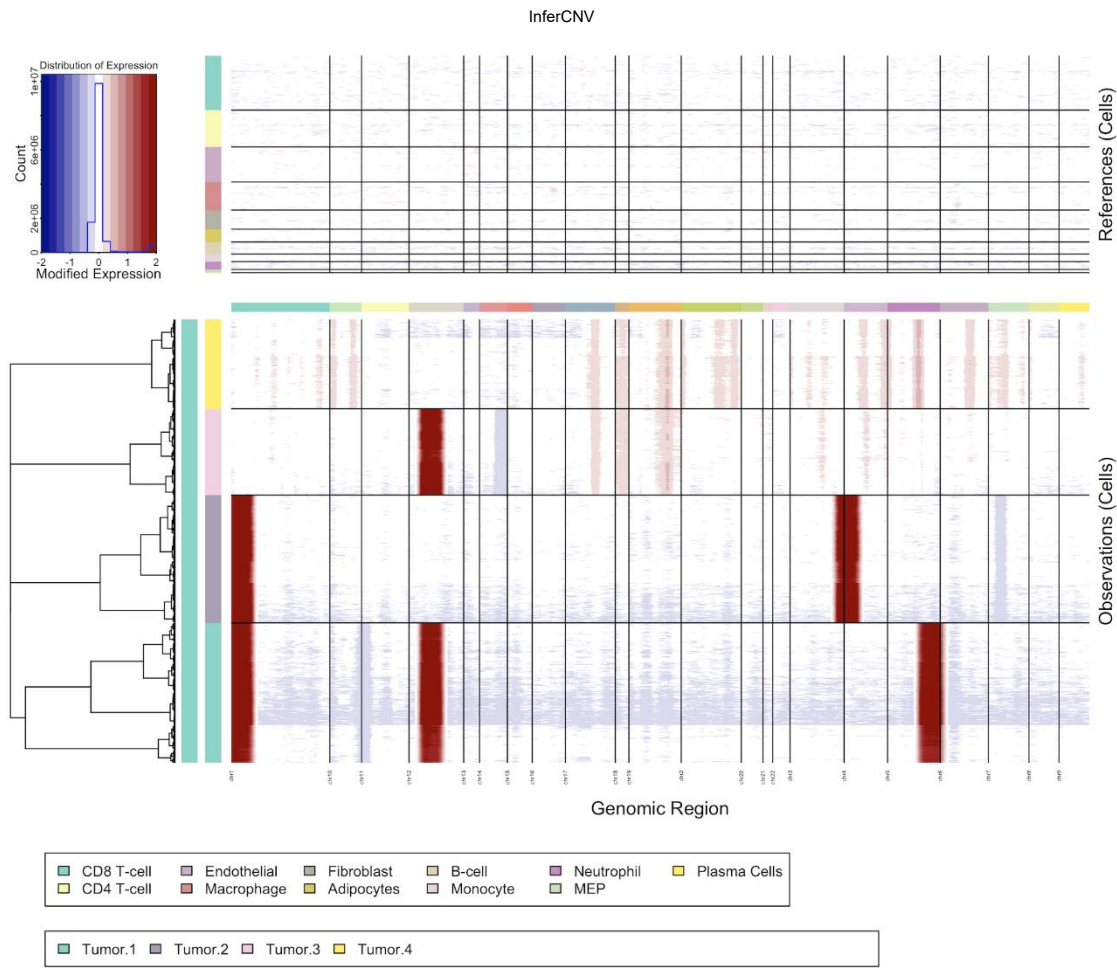
Extended Data Figure 3

It is made available under a [CC-BY-NC-ND 4.0 International license](https://creativecommons.org/licenses/by-nc-nd/4.0/).

A



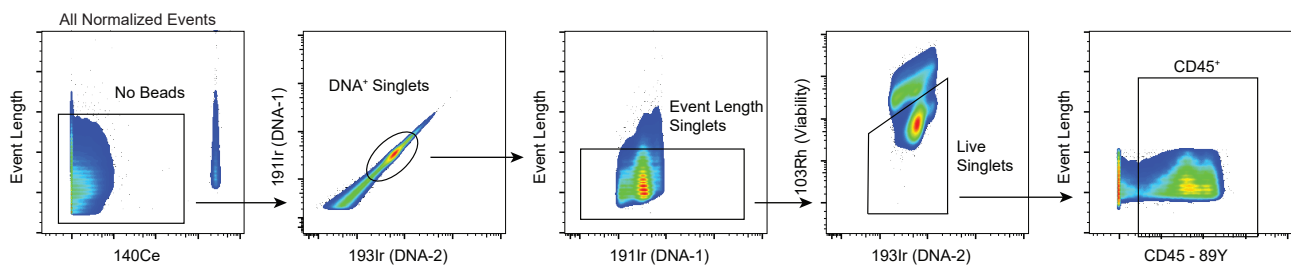
B



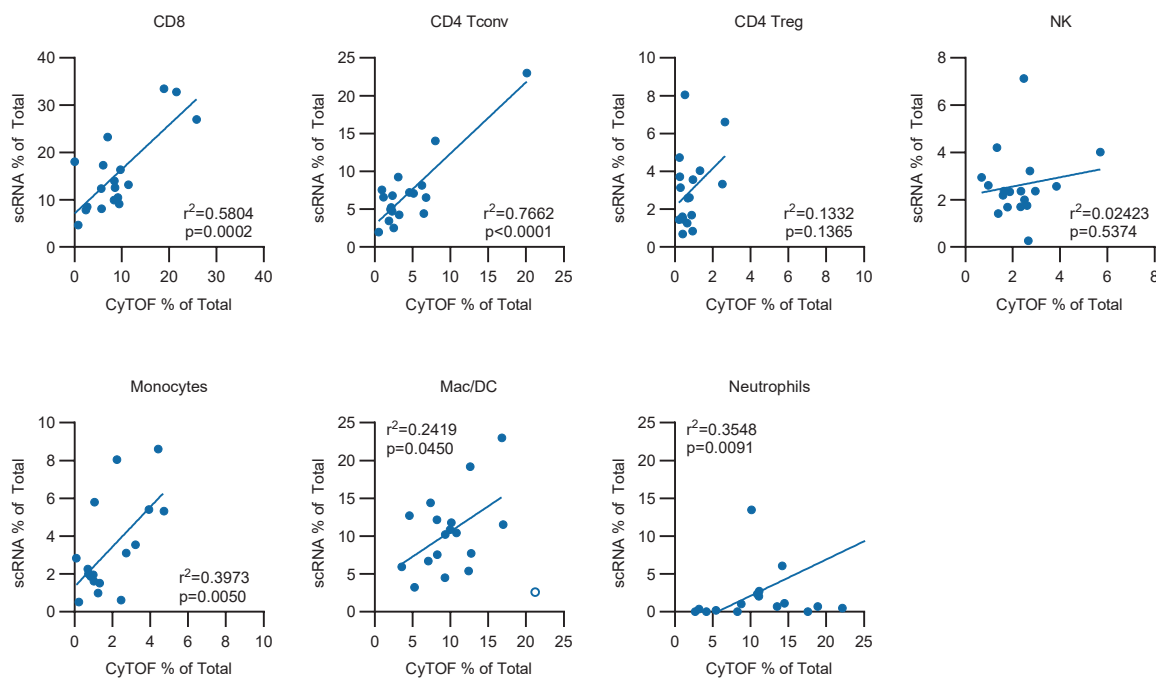
Extended Data Figure 4

It is made available under a [CC-BY-NC-ND 4.0 International license](https://creativecommons.org/licenses/by-nc-nd/4.0/).

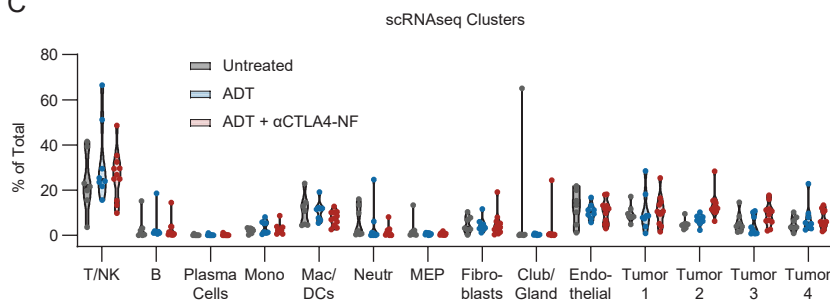
A



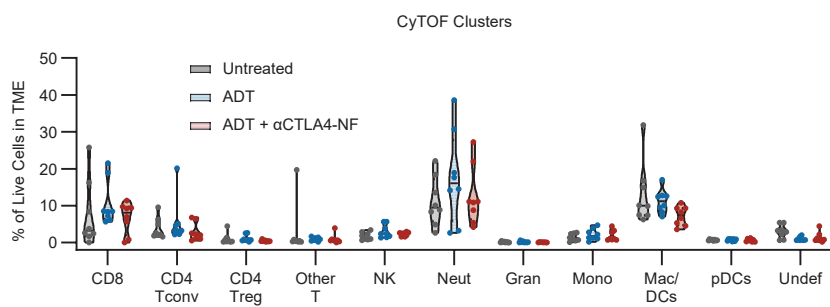
B



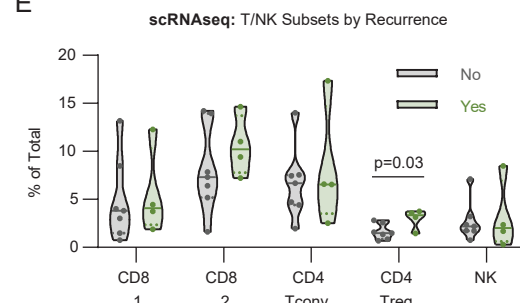
C



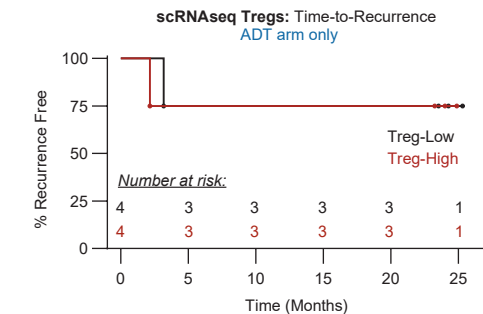
D



E

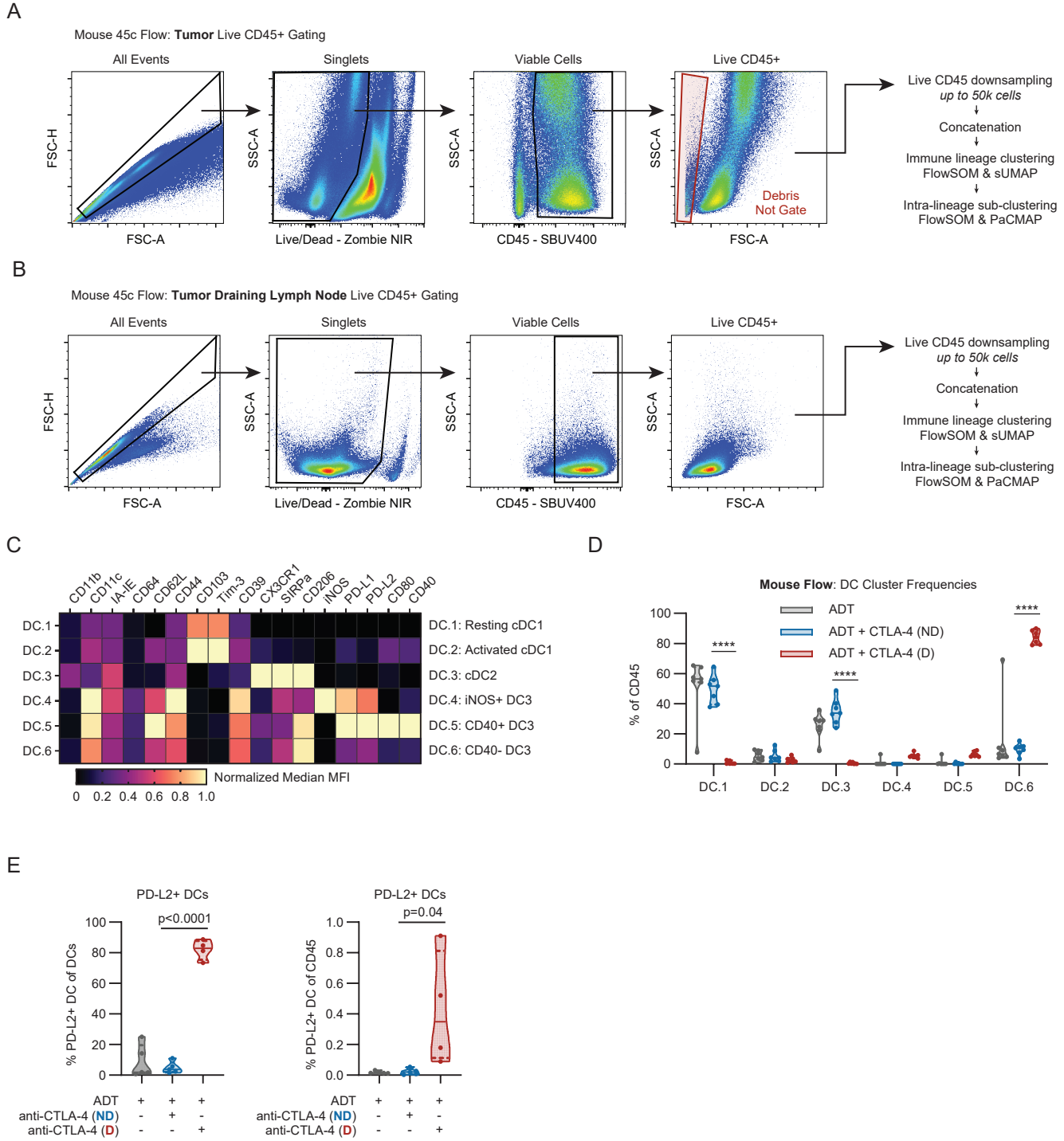


F



Extended Data Figure 5

It is made available under a [CC-BY-NC-ND 4.0 International license](https://creativecommons.org/licenses/by-nc-nd/4.0/).



Extended Data Figure 6

It is made available under a [CC-BY-NC-ND 4.0 International license](https://creativecommons.org/licenses/by-nc-nd/4.0/).

